

# Understanding the interplay of collagen and myocyte adaptation in cardiac volume overload: a multi-constituent growth and remodeling framework

Ludovica Maga<sup>a,b</sup>, Mathias Peirlinck<sup>a</sup>, Lise Noël<sup>b</sup>

<sup>a</sup>*Department of BioMechanical Engineering, Delft University of Technology, Delft, The Netherlands*

<sup>b</sup>*Department of Precision and Microsystems Engineering, Delft University of Technology, Delft, The Netherlands*

---

## Abstract

Hearts subjected to volume overload (VO) are prone to detrimental anatomical and functional changes in response to elevated mechanical stretches, ultimately leading to heart failure. Experimental findings increasingly emphasize that organ-scale changes following VO cannot be explained by myocyte growth alone, as traditionally proposed in the literature. Collagen degradation, in particular, has been associated with left ventricular adaptation in both acute and chronic stages of VO. These hypotheses remain to be substantiated by comprehensive mechanistic evidence, and the contribution of each constituent to myocardial growth and remodeling (G&R) processes is yet to be quantified. In this work, we establish a hybrid G&R framework in which we integrate a mixture-based constitutive model with the kinematic growth formulation. This multi-constituent model enables us to mechanistically assess the relative contributions of collagen and myocyte changes to alterations in tissue properties, ventricular dimensions, and growth phenotype. Our numerical results confirm that collagen dynamics control the passive mechanical response of the myocardium, whereas myocytes predominantly impact the extent and the phenotype of eccentric hypertrophy. Importantly, collagen degradation exacerbates myocyte hypertrophy, demonstrating a synergistic interplay that accelerates left ventricular progression toward diastolic dysfunction. This work constitutes an important step towards an integrated characterization of the early compensatory stages of VO-induced cardiac G&R.

*Keywords:* kinematic growth, constrained mixture theory, myocardial tissue, left ventricle model

---

## 1. Introduction

Heart failure is a prominent and life-threatening medical condition with an estimated incidence of 64 million people worldwide [1]. In this context, volume overload (VO) is a condition in which alterations to the mechanical loads develop because of a rise in preload, i.e., the stretch experienced by the cardiac wall at the end of diastole [2]. Sustained VO yields anatomical and functional changes, known as growth and remodeling (G&R), that are initially adaptive, allowing the organism to survive in an altered hemodynamic state. Nonetheless, when these compensatory mechanisms persist over time, they culminate in pathological changes that detrimentally affect the cardiac function, ultimately leading to heart failure [3, 4].

At the organ level, VO induces elevated cardiac wall stress and end-diastolic strain that promote rapid chamber dilation and a progressive increase in the end-diastolic volume ratio to wall thickness [5]. At the tissue level, VO promotes adaptation processes in myocardial cellular constituents, primarily myocytes, and extracellular matrix (ECM) components, primarily collagen [2, 6]. Cardiac myocytes account for 70% to 75% of the adult myocardium by cell volume and 25% to 30% by cell number, and are responsible for heart contraction and relaxation. Within myocytes, the contractile force is produced by organized functional units, the sarcomeres. The ECM embeds cardiac cells, providing structural support to the myocardium and is dynamically regulated by mechanical stress, neuro-hormonal signaling, and inflammation [7]. Collagen fibers

serve as the principal structural proteins within the ECM network. The functions attributed to ECM collagen include the provision of scaffolding for myocardial cells, the regulation of mechanical force transmission, and the determination of the systolic and diastolic stiffness of the ventricular chamber [8]. In response to myocardial overstretch, cardiomyocytes deposit sarcomeres in series, leading to lengthening and eccentric hypertrophy [9]. With myocyte elongation, progressive VO is characterized by continuous ECM remodeling. Modifications in ECM collagen are principally associated with an imbalance between extracellular matrix proteins, the metalloproteinases (MMPs), and their inhibitors (TIMPs). A net increase in the MMPs/TIMPs ratio favors collagen degradation and, consequently, loss of structural support, reduction in stiffness, wall thinning, and ultimately ventricular dilation [10, 11, 4].

Several investigations aimed at elucidating myocyte growth and ECM remodeling pathways in VO animal models. Experimental work by [12] demonstrated that volume overload caused by mitral regurgitation promotes extensive ECM remodeling due to a disproportionate increase in the MMPs/TIMPs ratio. Furthermore, they concluded that increased myocardial compliance results primarily from the collagen breakdown by MMPs, with minimal early contribution from cardiomyocyte growth. Studies on aortocaval fistula have led to similar conclusions [4, 8]. In their work, [13] found that interstitial collagen loss mediates rapid chamber dilatation, independently of structural and functional alterations in cardiomyocytes. In a second stage, the left ventricular diameter-to-thickness ratio decreases, the cardiomyocytes lengthen, further exacerbating the adverse eccentric remodeling. These observations indicate that both cardiomyocyte adaptation and ECM remodeling are pivotal to the course of G&R, as their interaction may dictate myocardial tissue adaptation during both early and late stages [13, 4]. Taken together, these findings emphasize that accounting for the interplay between tissue constituents is essential to fully characterize the progression of ventricular G&R. Understanding this interplay is key to elucidating the mechanobiological processes in VO and to guiding the development of targeted interventions to mitigate its adverse effects [14].

Computational modeling provides a powerful framework to investigate these interacting structure-function processes mechanistically, revealing how local changes in tissue microstructure translate into global alterations of organ function and vice versa [15, 16]. The vast majority of cardiac models of VO rely on the theory of kinematic growth [17, 18, 19, 20]. Here, the volumetric adaptation of the tissue is modeled through a multiplicative decomposition of the total deformation gradient into an inelastic part and an elastic part [21]. Growth kinematics are entirely specified by the inelastic deformation, where growth accommodates the serial addition of sarcomeres in myocytes [20]. Unfortunately, such phenomenological laws cannot accurately capture the interplay between G&R processes associated with individual tissue constituents [16]. Consequently, they are effective in capturing eccentric hypertrophy resulting from cardiomyocyte elongation, but they do not account for the underlying functional impact of collagen remodeling processes. Towards this gap, constrained mixture (CM) theory forms an interesting alternative approach to model and track G&R in soft biological tissues. In the CM framework, each tissue constituent has its own distinct deposition and removal rates, and the mixture of those constituents is bound to deform within a single continuum. Despite its more biologically mechanistic nature, the CM framework poses important practical challenges in terms of computational complexity. In fact, each individual evolving reference configuration needs to be tracked over time, which is costly. Reducing the computational expense of CM models has motivated the development of homogenized CM formulations [22], and remains an active area of ongoing research [23]. Moreover, CM is highly sensitive to constituent-specific deposition stretches, which can hardly be retrieved experimentally, unlike parameters such as initial fractions and growth rates that can be quantified histologically or calibrated [24]. Such limitations have hindered its extension to three-dimensional models [25], [26]. Although CM has been largely applied in the context of vascular tissues, its suitability for cardiac G&R has only been scarcely explored to date [27, 28].

This work proposes a novel hybrid G&R computational framework that integrates a multi-constituent tissue representation with the kinematic growth theory, accounting for different volume and density adaptations of individual cardiac constituents. Instead of tracking growth through the evolution of a single growth multiplier, as is done in the vast majority of cardiac G&R numerical studies [15, 19, 16], we introduce distinct G&R of microstructural constituents at both kinematic and constitutive levels, as first outlined in

[29]. Hereby, mass changes in tissue constituents are described by volume or density adaptation: constituent-specific volume changes add up to the global volumetric change of the mixture. This kinematic coupling of mass change and volume adaptation is entirely achieved by defining the growth deformation gradient tensor, as done in standard kinematic growth formulation. With this study, we aim to establish a G&R multi-constituent framework that links anatomical and functional myocardial changes to myocyte and collagen adaptation. We employ this framework to predict the intrinsic processes occurring in myocardial tissue under VO and to quantify the individual contributions of microstructural mechanisms and their combined effects in the progression of VO-induced adaptation.

## 2. Mechanics of multi-constituent tissue

To characterize the adaptation processes of myocardial tissue during pathologic G&R, we propose a framework that integrates theoretical concepts of finite strain theory, soft tissue constitutive modeling, and G&R formulations. The subsequent sections detail the relevant governing equations for G&R, starting with the kinematic and the balance equations in Subsections 2.1 and 2.2. In Subsection 2.3, we describe the passive material response based on the definition of the total Helmholtz free energy. Subsection 2.5 extends the framework to a multi-constituent description of the tissue based on the theory of mixture, including components such as collagen fibers, myocytes, and ECM. Such a description allows for capturing any change in mass, modeled as volume or density adaptation for each constituent.

### 2.1. Kinematics

In a three-dimensional domain, the mapping  $\varphi(\mathbf{X}) = \mathbf{x}$ , relates the location  $\mathbf{X}$  of a point in the reference configuration  $\Omega_0$  at time  $t = 0$  to its location  $\mathbf{x}$  in a deformed configuration  $\Omega_t$  at time  $t$ . The deformation gradient,  $\mathbf{F} = \partial\mathbf{x}/\partial\mathbf{X}$ , relates the undeformed and deformed vectors,  $d\mathbf{X}$  and  $d\mathbf{x}$ , respectively, and its determinant,  $\det\mathbf{F} = J$ , accounts for volume changes. This definition leads to the derivation of the right Cauchy-Green  $\mathbf{C}$  and the left Cauchy-Green tensors  $\mathbf{b}$ ,

$$\mathbf{C} = \mathbf{F}^\top \mathbf{F}, \quad \mathbf{b} = \mathbf{F} \mathbf{F}^\top. \quad (1)$$

#### 2.1.1. Kinematics of growth

To account for both the volume adaptation, occurring over the G&R time  $s$ , and the elastic response, associated with the short time scale, the deformation gradient tensor is decoupled into a growing part and an elastic part [21],

$$\mathbf{F} = \mathbf{F}^e(t) \mathbf{F}^g(\tau). \quad (2)$$

Growth and remodeling change the stress-free reference configuration of the tissue,  $\Omega_0$ , leading, in general, to a mechanically *incompatible* configuration,  $\Omega_\tau$ , introduced through the inelastic growth deformation gradient tensor  $\mathbf{F}^g$ . The geometric and elastic compatibility is restored by the elastic deformation gradient tensor  $\mathbf{F}^e$ , which generates residual stresses and strains [30]. Figure 1 provides a schematic illustration of the growth kinematics. The elastic right Cauchy-Green tensor is introduced:

$$\mathbf{C}^e = \mathbf{F}^{e\top} \cdot \mathbf{F}^e = \mathbf{F}^{g\top} \cdot \mathbf{C} \cdot \mathbf{F}^{g-1}. \quad (3)$$

The growth deformation gradient tensor accommodates any volume change with respect to the initial time  $s = 0$  before any G&R, while the elastic deformation tensor is restricted to near-incompressibility. We omit the time dependency of the tensor in the following sections for conciseness.

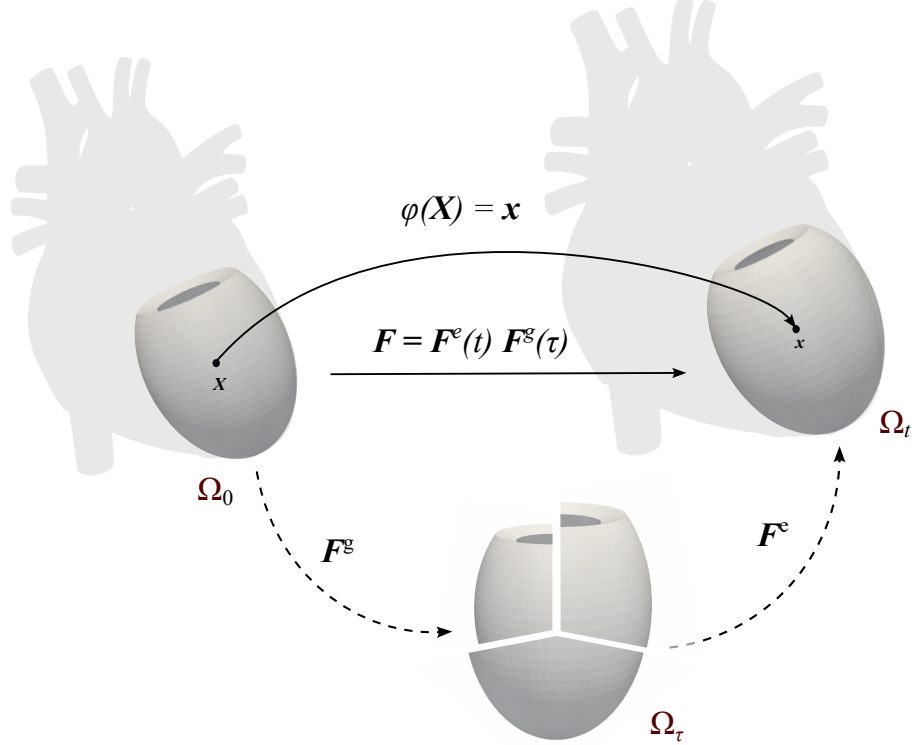


Figure 1: **Kinematics of cardiac growth.** A point located at  $\mathbf{X}$  in the reference configuration  $\Omega_0$  is mapped to the current configuration through the motion  $\varphi(\mathbf{X})$  and undergoes a total deformation characterized by the deformation gradient  $\mathbf{F}$ . The total deformation is multiplicatively decomposed into the growth part  $\mathbf{F}^g$  and the elastic part  $\mathbf{F}^e$ , such that  $\mathbf{F} = \mathbf{F}^e \mathbf{F}^g$ . Growth induces an intermediate, stress-free configuration in which the tissue expands locally without mechanical constraints, possibly creating overlaps and incompatibilities. The resulting mechanically incompatible configuration,  $\Omega_\tau$ , is followed by the elastic deformation  $\mathbf{F}^e$ , which restores tissue continuity and leads to the residually stressed configuration  $\Omega_t$ .

### 2.1.2. Kinematics of near-incompressibility

Myocardial tissue is often assumed incompressible, which means that its volume is preserved during elastic deformation. However, experimental measurements have shown changes in wall volume up to 10%, indicating that myocardial tissue exhibits near-incompressibility [15]. We enforce the condition of near-incompressibility through an additional split of the elastic deformation gradient tensor  $\mathbf{F}^e$  into its volumetric  $\mathbf{F}_{\text{vol}}$  and isochoric part  $\bar{\mathbf{F}}$ :

$$\mathbf{F}^e = \mathbf{F}_{\text{vol}} \bar{\mathbf{F}}, \quad (4)$$

where

$$\mathbf{F}_{\text{vol}} = (J^e)^{1/3} \mathbf{I}, \quad \bar{\mathbf{F}} = (J^e)^{-1/3} \mathbf{F}^e, \quad (5)$$

implying that  $J = \det \mathbf{F}$  and  $\det \bar{\mathbf{F}} \equiv 1$ .

Thus, the elastic right Cauchy–Green deformation tensor can be further decoupled into its isochoric and volumetric parts,  $\mathbf{C}^e = \mathbf{F}^{e^\top} \mathbf{F}^e = (J^e)^{2/3} \bar{\mathbf{C}}$ . Accordingly, the isochoric invariants are given as  $\bar{I}_1 = \text{tr} \bar{\mathbf{C}}$ , and  $\bar{I}_3 = \det \bar{\mathbf{C}} \equiv 1$ . The pseudo-invariant denoted  $\bar{I}_4 = \bar{\mathbf{C}} : \mathbf{N}$ , with  $\mathbf{N} = \mathbf{n} \otimes \mathbf{n}$ , the structural tensor defined by the characteristic material direction  $\mathbf{n}$ . Tensor product notations are introduced for the dyadic product  $\{\bullet \otimes \circ\}_{ij} = \{\bullet\}_i \{\circ\}_j$ , and the double contraction operation  $\{\bullet : \circ\} = \{\bullet\}_{ij} \{\circ\}_{ij}$ . Incompressibility is achieved by introducing a penalty function in the material model, such that the determinant of the elastic deformation gradient tensor tends to 1, see Subsection 2.3.2.

## 2.2. Balance of Linear Momentum

Given that G&R processes typically occur on a time scale of days, weeks, or months, and elastic deformation occurs on time scales of seconds or less, we can adopt the *slow growth* assumption and consider our mechanical system to be quasi-static [30]. Denoting the body force vector as  $\mathbf{B}_0$ , the balance of linear momentum in the reference configuration can be expressed as:

$$\text{Div}(\mathbf{P}) + \mathbf{B}_0 = \mathbf{0}, \quad (6)$$

with  $\mathbf{P}$  the first Piola-Kirchhoff stress tensor, and  $\text{Div}(\cdot)$  denoting the divergence operator.

## 2.3. Constitutive model

The non-linear constitutive behavior of myocardial tissue is considered hyperelastic and defined by a strain energy density function. The total tissue deformation depends on both the elastic and growth components. Herein, Subsection 2.3.1 describes the hyperelastic material model by specifying the total stress and tangent moduli. In Subsection 2.3.2, the free energy function is split into a volumetric and an isochoric part, and the constitutive equations are reformulated accordingly.

### 2.3.1. Constitutive equations of growth

We introduce the Helmholtz free energy function  $\psi$ , defined per unit volume, and embed the growth kinematics, outlined in Section 2.1. This allows writing the total second Piola-Kirchhoff stress as:

$$\mathbf{S} = 2 \frac{\partial \psi}{\partial \mathbf{C}} = 2 \frac{\partial \psi}{\partial \mathbf{C}^e} : \frac{\partial \mathbf{C}^e}{\partial \mathbf{C}} = \mathbf{F}^{g-1} \cdot \mathbf{S}^e \cdot \mathbf{F}^{g-\top}. \quad (7)$$

The fourth-order tangent modulus is given by the total derivative of the second Piola-Kirchhoff stress with respect to the right Cauchy-Green deformation tensor:

$$\mathbb{C} = 2 \frac{d\mathbf{S}}{d\mathbf{C}} = \mathbb{C}^e + \mathbb{C}^g = 2 \frac{\partial \mathbf{S}}{\partial \mathbf{C}} \Big|_{\mathbf{F}^g} + 2 \frac{\partial \mathbf{S}}{\partial \mathbf{C}} \Big|_{\mathbf{F}}. \quad (8)$$

The first term can be written as:

$$\mathbb{C}^e = 2 \frac{d\mathbf{S}}{d\mathbf{C}} \Big|_{\mathbf{F}^g} = (\mathbf{F}^{g-1} \overline{\otimes} \mathbf{F}^{g-1}) : 2 \frac{\partial \mathbf{S}^e}{\partial \mathbf{C}^e} : (\mathbf{F}^{g-\top} \overline{\otimes} \mathbf{F}^{g-\top}), \quad (9)$$

where  $\partial \mathbf{S}^e / \partial \mathbf{C}^e$  is the elastic tangent modulus. The following notation  $\{\bullet \overline{\otimes} \circ\}_{ijkl} = \{\bullet\}_{ik} \{\circ\}_{jl}$  is introduced for the tensor multiplication. Using the chain rule, the second term can be further written as:

$$\mathbb{C}^g = 2 \frac{d\mathbf{S}}{d\mathbf{C}} \Big|_{\mathbf{F}} = 2 \frac{\partial \mathbf{S}}{\partial \mathbf{F}^g} : \frac{\partial \mathbf{F}^g}{\partial \mathbf{C}}. \quad (10)$$

Note that the last term of Eq. (10) is dependent on the specific choice for the growth evolution equations of  $\mathbf{F}^g$  [15], detailed in Section 3.4. For simplicity, a common choice is to adopt an explicit time integration for the growth deformation gradient tensor  $\mathbf{F}_g$  (i.e.,  $\mathbf{F}_g^{n+1}$  is independent of the total strain tensor  $\mathbf{C}^{n+1}$ ) [31, 32, 33]. The computation of the tangent modulus thus reduces to Eq. (9). In practice, given a specific choice for  $\psi$  and for  $\mathbf{F}^g$ , the computation of the elasticity tensor requires calculating  $\mathbf{S}^e$  and its derivative with respect to  $\mathbf{C}^e$ .

### 2.3.2. Constitutive equations of near-incompressibility

The kinematic decoupling of the elastic deformation gradient tensor in Eq. (4) allows for the additive split of the strain energy density function into an isochoric and a volumetric contribution,

$$\psi = \psi_{\text{vol}}(J) + \bar{\psi}(\bar{\mathbf{C}}). \quad (11)$$

The first is commonly associated with the presence of water in biological tissue, while the second is defined on the basis of the material microstructure. In this work, the volumetric term chosen to enforce near-incompressibility is defined as:

$$\psi_{\text{vol}} = \frac{\mu}{2}(J^e - 1)^2, \quad (12)$$

where  $\mu$  acts as a penalty parameter. The elastic Second Piola-Kirchhoff stress is then defined in terms of its volumetric and isochoric parts as:

$$\mathbf{S}^e = 2 \frac{\partial \psi(\mathbf{C}^e)}{\partial \mathbf{C}^e} = \mathbf{S}_{\text{vol}} + \mathbf{S}_{\text{iso}}. \quad (13)$$

The volumetric contribution is computed as

$$\mathbf{S}_{\text{vol}} = 2 \frac{\partial \psi_{\text{vol}}(J^e)}{\partial \mathbf{C}^e} = 2 \frac{\partial \psi_{\text{vol}}(J^e)}{\partial J^e} \cdot \frac{\partial J^e}{\partial \mathbf{C}^e}, \quad (14)$$

and the isochoric contribution is defined as:

$$\mathbf{S}_{\text{iso}} = 2 \frac{\partial \bar{\psi}(\bar{\mathbf{C}})}{\partial \mathbf{C}^e} = 2 \frac{\partial \bar{\psi}(\bar{\mathbf{C}})}{\partial \bar{\mathbf{C}}} \cdot \frac{\partial \bar{\mathbf{C}}}{\partial \mathbf{C}^e}. \quad (15)$$

Analogously, the derivative of the elastic second Piola-Kirchhoff stress with respect to the right-Cauchy strain tensor can be decoupled into:

$$\mathbb{C}^e = 2 \frac{\partial \mathbf{S}^e}{\partial \mathbf{C}^e} = 4 \frac{\partial^2 \psi(\mathbf{C}^e)}{\partial \mathbf{C}^e \partial \mathbf{C}^e} = \mathbb{C}_{\text{vol}} + \mathbb{C}_{\text{iso}}, \quad (16)$$

where the volumetric and isochoric part can be further specified following [34]:

$$\mathbb{C}_{\text{vol}} = 2 \frac{\partial \mathbf{S}_{\text{vol}}}{\partial \mathbf{C}^e} = 4 \frac{\partial^2 \psi_{\text{vol}}(J^e)}{\partial \mathbf{C}^e \partial \mathbf{C}^e}, \quad (17)$$

$$\mathbb{C}_{\text{iso}} = 2 \frac{\partial \mathbf{S}_{\text{iso}}}{\partial \mathbf{C}^e} = 4 \frac{\partial^2 \bar{\psi}(\bar{\mathbf{C}})}{\partial \mathbf{C}^e \partial \mathbf{C}^e}. \quad (18)$$

The full derivation of the volumetric and isochoric part of the fourth-order elasticity tensors is provided in **Appendix C**.

### 2.4. Mixture model

Myocardial tissue is modeled as a mixture of  $I$  constituents that are constrained to follow the deformation of the continuum. At a material point, all constituents are simultaneously present. On a short time scale,  $t$ , the tissue is considered nearly-incompressible; however, on a longer time scale,  $\tau$ , it may experience a change in volume due to an increase or decrease in mass. The multi-constituent representation allows for changes in individual mass and volume to contribute to the total change of volume of the tissue,  $V$  [29]. For each constituent, we introduce the volume  $V_i$ , the mass  $m_i$ , the volume fractions  $\phi_i$ , and the partial and individual densities,  $\rho_i$  and  $r_i$ , respectively. At time  $s = 0$ , the latter are defined as

$$\rho_i^0 = \frac{m_i^0}{V^0}, \quad r_i^0 = \frac{m_i^0}{V_i^0}. \quad (19)$$

At the current G&R time  $s$ , we define the normalized mass  $\hat{m}_i$ , volume  $\hat{v}_i$ , and the partial  $\hat{\rho}_i$  and individual  $\hat{r}_i$  densities for each constituent defined with respect to the initial state:

$$\hat{m}_i = \frac{m_i}{m_i^0}, \quad \hat{v}_i = \frac{V_i}{V_i^0}, \quad \hat{\rho}_i = \frac{\rho_i}{\rho_i^0}, \quad \hat{r}_i = \frac{r_i}{r_i^0}. \quad (20)$$

By using those definitions, the strain energy function can be written as the sum of constituent-specific strain energy functions, each weighted by the partial mass density:

$$\bar{\psi}(\bar{\mathbf{C}}) = \sum_{i=1}^N \hat{\rho}_i \bar{\psi}_i. \quad (21)$$

This assumption was postulated by [22] in the context of a constrained mixture. Within the mixture, each constituent follows the same deformation, and thus, the stress-strain equations read:

$$\mathbf{S}_{\text{iso}} = 2 \frac{\partial \bar{\psi}(\bar{\mathbf{C}})}{\partial \mathbf{C}^e} = 2 \sum_{i=1}^I \hat{\rho}_i \frac{\partial \bar{\psi}_i(\bar{\mathbf{C}})}{\partial \mathbf{C}^e}, \quad (22)$$

$$\mathbb{C}_{\text{iso}} = 2 \frac{\partial \mathbf{S}_{\text{iso}}(\bar{\mathbf{C}})}{\partial \mathbf{C}^e} = 4 \sum_{i=1}^I \hat{\rho}_i \frac{\partial^2 \bar{\psi}_i(\bar{\mathbf{C}})}{\partial \mathbf{C}^e \partial \mathbf{C}^e}. \quad (23)$$

The specific choice for the constituents' strain energy function is presented in Section 3.

### 2.5. Growth and Remodeling - Volume adaptation versus density adaptation

Following a similar approach to vascular remodeling studies [35, 36], we assume that a constituent mass change results in either a change in volume or in density for that constituent. For volume adaptation (VA), the individual density is constant and the individual volume changes, while for density adaptation (DA), the individual density is adaptive and the individual volume is constant. The hypotheses regarding VA and DA for each constituent are substantiated by mechanobiological considerations in Section 3.

In the VA scenario, the individual mass density remains constant during G&R, i.e.,  $r_i \equiv r_i^0$ . Therefore, we can write:

$$\hat{m}_i = \frac{m_i}{m_i^0} = \frac{r_i V_i}{r_i^0 V_i^0} = \frac{V_i}{V_i^0} = \hat{v}_i. \quad (24)$$

According to the definition in [35], the partial density change can then be written as:

$$\hat{\rho}_i = \frac{\rho_i}{\rho_i^0} = \frac{m_i V^0}{m_i^0 V} = \hat{m}_i \cdot \frac{1}{\hat{v}} = \hat{v}_i \cdot \frac{1}{\hat{v}}. \quad (25)$$

DA scenario means that the constituent-specific mass change is attributed to pure alterations in individual mass density, not affecting the individual volume, i.e.,  $V_i \equiv V_i^0$ , and it follows that:

$$\hat{m}_i = \frac{m_i}{m_i^0} = \frac{r_i V_i}{r_i^0 V_i^0} = \frac{r_i}{r_i^0} = \hat{r}_i. \quad (26)$$

Similarly to the previous case, see Eq.(25), the individual mass density change can then be written as:

$$\hat{\rho}_i = \hat{r}_i \cdot \frac{1}{\hat{v}}. \quad (27)$$

Pure tissue volume growth occurs when all constituents follow VA, whereas pure tissue density remodeling occurs when all constituents follow DA. In contrast, if some constituents follow VA and others follow DA, the volume change of the whole tissue results as follows:

$$\dot{v} = \frac{V}{V^0} = \sum_{i=1}^I \frac{V_i}{V_i^0} = \sum_{i=1}^I \frac{V_i}{V^0} \frac{V_i^0}{V_i^0} = \sum_{i=1}^N \hat{v}_i \phi_i^0 = \sum_{i_{\text{VA}}} \hat{m}_i \phi_i^0 + \sum_{i_{\text{DA}}} \phi_i^0. \quad (28)$$

where  $\hat{v}_i \equiv 1$  if the constituent  $i$  follows DA and  $\hat{v}_i \equiv \hat{m}_i$  if it follows VA. The normalized density keeps the generic form:

$$\hat{\rho}_i = \hat{m}_i \cdot \frac{1}{\hat{v}}. \quad (29)$$

The change in tissue volume  $\hat{v}$  resulting from the individual change in mass of constituents specifies the growth kinematics according to the theory of kinematic growth [21]. The growth deformation gradient tensor introduced in Section 2.1.1, describes the total change in volume occurring at any G&R time  $\tau$ , through:

$$\det \mathbf{F}^g = \hat{v}. \quad (30)$$

G&R is, thus, modeled such that the change in tissue volume  $\hat{v}$  specifies growth kinematics, while partial density changes  $\hat{\rho}_i$  of individual constituents  $i$  are used to connect the adaptation of the tissue to its elastic response.

Mass growth is typically coupled to a mechanical stimulus through an evolution equation that dictates the rate at which growth occurs over a long timescale. The dependency on the mechanical driving force usually involves mechanical stress or strain, which are used to define the homeostatic state, i.e., the preferred state at which the tissue is at equilibrium. A generic mass evolution equation can be given as:

$$\frac{\partial \hat{m}_i}{\partial \tau} (\hat{m}_i, \bar{\mathbf{S}}, \bar{\mathbf{C}}) = \kappa_i \xi_i (\hat{m}_i, \bar{\mathbf{S}}, \bar{\mathbf{C}}), \quad (31)$$

where the growth criterion function  $\xi_i$  for a constituent  $i$  is defined to promote the restoration to the homeostatic state. The temporal evolution is determined by the growth gain constant  $\kappa_i$ . The stimulus can be written in a generic form as:

$$\xi_i = \langle g(\bar{\mathbf{S}}, \bar{\mathbf{C}}) - g_{\text{hom}} \rangle, \quad (32)$$

Where  $g$  is a mechanical driving force, dependent on stress or strain. The Macaulay brackets are introduced, ensuring that growth is activated only in the case of positive stimulus:

$$\langle g(\bar{\mathbf{S}}, \bar{\mathbf{C}}) - g_{\text{hom}} \rangle = \begin{cases} g(\bar{\mathbf{S}}, \bar{\mathbf{C}}) - g_{\text{hom}}, & \text{if } g(\bar{\mathbf{S}}, \bar{\mathbf{C}}) - g_{\text{hom}} > 0, \\ 0, & \text{if } g(\bar{\mathbf{S}}, \bar{\mathbf{C}}) - g_{\text{hom}} \leq 0. \end{cases} \quad (33)$$

### 3. Myocardial tissue model

The generic constitutive framework introduced in Section 2.3 is now specialized to represent the behavior of myocardial tissue as a mixture. In the following sections, we briefly summarize the key morphological characteristics of the myocardium and its principal structural constituents. In Subsection 3.1, we define the strain energy density functions associated with each constituent. The choice of the growth deformation gradient tensor is specified in Subsection 3.2, formulated to capture the eccentric remodeling pattern observed at the organ level under VO conditions. Subsection 3.4 outlines the evolution equations governing mass growth for each myocardial constituent, including mechanically-driven stimuli acting as the G&R driving factors.

#### 3.1. Constitutive model

Among myocardial tissue constituents, myocytes and collagen fibers dominate the mechanical response of the tissue [22]. Consequently, we propose a mixture-based constitutive model that considers the stress-strain response of these two constituents. The remaining tissue components are grouped into a ground matrix constituent, which predominantly contains elastin. Without loss of generality, we focus on the tissue's passive mechanical behavior for now. Building on the well-established orthotropic model of the myocardium introduced by [37], we define a microstructural-informed strain energy functions representing the tissue's

intrinsic mixture of myocytes and collagen. Before any G&R has taken place, i.e., at time  $s = 0$ , the material response must reproduce the baseline behavior captured on healthy tissue [38].

Histologically, the left ventricular myocardium is a layered composite structure made of myocytes and a network of collagen fibers embedded in the ground matrix [39, 40, 41]. This organized architecture of myocardial layers, or *sheets*, provides a natural reference to define an orthonormal set of material directions. The local basis vectors include the fiber direction,  $\mathbf{f}_0$ , which aligns with the longitudinal axis of myocytes, the sheet direction,  $\mathbf{s}_0$ , which lies within the transmural plane, and the sheet-normal direction,  $\mathbf{n}_0$ , which is orthogonal to both  $\mathbf{f}_0$  and  $\mathbf{s}_0$ . Regarding the collagen network, different fiber families, often referred to as *endomysial* and *perimysial* collagen, form lateral connections both between adjacent myocytes and sheets.

The isochoric mechanical response of myocardial tissue is obtained by the additive contributions of the strain energy functions associated with myocardial constituents, i.e., myocytes, collagen fibers, and ground matrix.

$$\bar{\psi}(\bar{\mathbf{C}}) = \sum_{i=1}^I \hat{\rho}_i \bar{\psi}_i = \hat{\rho}_g \bar{\psi}_g + \hat{\rho}_m \bar{\psi}_m + \hat{\rho}_c \bar{\psi}_c, \quad (34)$$

where we distinguish between myocytes,  $i = m$ , collagen network,  $i = c$  and ground matrix,  $i = g$ .

**Myocytes.** Myocytes are assumed to bear loading along their principal direction [42, 28], and therefore, the associated strain energy consists of a one-dimensional exponential term:

$$\bar{\psi}_m = \frac{a_m}{2b_m} \{ \exp[b_m(\bar{I}_{4m}^* - 1)^2] - 1 \}, \quad (35)$$

where  $\bar{I}_{4m}^* = \max\{\bar{I}_{4m}, 1\}$  and  $\bar{I}_{4m} = \mathbf{f}_0 \cdot \bar{\mathbf{C}} \mathbf{f}_0$  is the isochoric fourth pseudo-invariant, where we further assume that myocytes start to bear the load only when they are stretched.  $\mathbf{f}_0$  denotes the preferred direction of myocytes in the reference configuration.

**Collagen.** Collagen forms a fibrous network that envelopes the myocytes. Image-based characterization of the architecture of myocardial collagen by [39, 43] suggests a distinction between endomysial and perimysial collagen fiber. The endomysial collagen network is organized in two fiber families: one family surrounds individual myocytes and contributes to load bearing along the principal fiber direction,  $\mathbf{f}_0$ , and the second family forms lateral connections between myocytes and is assumed to align with the sheet direction,  $\mathbf{s}_0$ . The perimysial collagen fiber, in their turn, connect the different sheetlets together, and as such act along the sheet-normal direction,  $\mathbf{n}_0$ . Furthermore, the microstructural organization of myocardial tissue motivates us to assume an additional collagenous shear interaction strain energy contribution in the fiber-sheet plane, in line with the shear contribution assumed in [37], and further adopted by [42]. This brings us to a four-term strain energy function describing the collagen fiber network contribution to the strain energy function:

$$\begin{aligned} \bar{\psi}_c = & \frac{a_{cf}}{2b_{cf}} \{ \exp[b_{cf}(\bar{I}_{4cf}^* - 1)^2] - 1 \} + \frac{a_{cs}}{2b_{cs}} \{ \exp[b_{cs}(\bar{I}_{4cs}^* - 1)^2] - 1 \} + \frac{a_{cn}}{2b_{cn}} \{ \exp[b_{cn}(\bar{I}_{4cn}^* - 1)^2] - 1 \} \\ & + \frac{a_{cfs}}{2b_{cfs}} \{ \exp[b_{cfs}(\bar{I}_{8cfs})^2] - 1 \}, \end{aligned} \quad (36)$$

where  $\bar{I}_{4f} = \mathbf{f}_0 \cdot \bar{\mathbf{C}} \mathbf{f}_0$ ,  $\bar{I}_{4s} = \mathbf{s}_0 \cdot \bar{\mathbf{C}} \mathbf{s}_0$ ,  $\bar{I}_{4n} = \mathbf{n}_0 \cdot \bar{\mathbf{C}} \mathbf{n}_0$ , are the isochoric pseudo-invariants that contain the material directions  $\mathbf{f}_0$ ,  $\mathbf{s}_0$ ,  $\mathbf{n}_0$ , and  $\bar{I}_{4cf}^* = \max\{\bar{I}_{4cf}, 1\}$ ,  $\bar{I}_{4cs}^* = \max\{\bar{I}_{4cs}, 1\}$ ,  $\bar{I}_{4cn}^* = \max\{\bar{I}_{4cn}, 1\}$ , ensuring that only the stretched fibers can bear the load passively. Having limited  $\bar{I}_{4cf}, \bar{I}_{4cs}, \bar{I}_{4cn} \geq 1$  and  $\bar{I}_{4m} \geq 1$  the strain energy functions always meet the requirements of convexity and ellipticity [34]. The fourth term includes the coupling invariant  $\bar{I}_{8fs} = \mathbf{f}_0 \cdot \bar{\mathbf{C}} \mathbf{s}_0$ .

**Ground matrix.** The remaining myocardial constituents, primarily elastin, are uniformly distributed within the myocardium [42, 40, 44] and thus are often modeled as incompressible and isotropic material [45]. The ground matrix strain energy function is chosen as:

$$\bar{\psi}_g = \frac{a_g}{2b_g} \{ \exp[b_g(\bar{I}_1 - 3)] \}, \quad (37)$$

where  $a_g, b_g$  constitutive parameters. We observe that before any G&R has taken place, i.e. at time  $s = 0$ , the mixture-based model resembles the generalized five-term constitutive model in [37], except for the contribution along the principal fiber direction between the one-dimensional myocytes and the collagen family oriented parallel to the myocytes' long axis, which are, here, decoupled. The interested reader is referred to **Appendix A** for the detailed derivation of the Second Piola-Kirchhoff stress and the elasticity tensor of the myocardial mixture.

### 3.2. Myocyte mass change

Myocytes primarily contribute to cardiac G&R through *hypertrophy*, wherein the cells increase in size, rather than *hyperplasia*, which involves an increase in the number of cells. This physiological behavior prompts myocyte constituent evolutions to be properly modeled following the VA-framework we disclosed in Section 2.5. It has been shown that elevated, non-homeostatic, diastolic tissue stretch serves as a predominant stimulus for G&R under VO conditions, both at the tissue and organ levels [20]. We incorporate this behavior by modeling myocyte mass changes following a stretch-driven evolution equation:

$$\frac{\partial \hat{m}_m}{\partial \tau} = \frac{\partial \hat{v}_m}{\partial \tau} = \kappa_m \hat{m}_m < \bar{\lambda}_m - \bar{\lambda}_{mf,hom} >, \quad (38)$$

where growth is activated if the elastic isochoric stretch,  $\bar{\lambda}_m = \mathbf{f}_0 \cdot \bar{\mathbf{F}}^\top \bar{\mathbf{F}} \cdot \mathbf{f}_0$ , exceeds a critical homeostatic stretch level  $\bar{\lambda}_{mf,hom}$ . Here,  $\kappa_m$  denotes the growth rate parameter that regulates the temporal speed at which myocytes grow.

### 3.3. Collagen mass change

Multiple studies have characterized the processes of collagen synthesis and degradation in various soft tissues [46, 47, 48]. In the myocardium, collagen turnover involves a complex cascade of mechanobiological subprocesses, including changes in extracellular matrix proteins and their regulation by cellular and mechanical cues, among other factors. Previous studies have successfully adopted phenomenological formulations to describe collagen deposition and degradation through alterations in collagen density [49, 50]. Following this work, we adopt our DA framework to model collagen mass changes. Other models, based on the constrained mixture framework, typically represent collagen turnover as the superposition of deposited and degraded mass, with the net mass production rate prescribed constitutively [28]. In this study, we do not explicitly model the continuous deposition and degradation of collagen; instead, we phenomenologically prescribe the net collagen mass change. Motivated by experimental observations under VO, we allow the collagen mass to decrease according to a decay function:

$$\hat{m}_c(\tau) = \hat{r}_c(\tau) = \hat{m}_{c,min} + [\hat{m}_c^0 - \hat{m}_{c,min}] \exp[-\frac{\tau}{\tau_{end}}], \quad (39)$$

with the growth parameter  $\tau_{end}$  denoting the G&R time  $s$  for the degradation of collagen to reach the minimal mass ratio  $\hat{m}_{c,min}$ .

It should be noted that this simplification holds in this case as we focus our analysis on the compensated stage of VO (limited to the first weeks of G&R [4]), which has been associated with a net decrease in collagen mass. Net collagen mass increase, instead, might occur in late stages, often referred to as *decompensated*, as an attempt to counterbalance the increased myocardial compliance [10]. Modeling the end-stage collagen deposition is out of our scope, and thus, our growth scenarios can be simplified through Eq. (39).

### 3.4. Volumetric tissue growth

Given our physiology-informed choices to model myocyte mass change following the VA-framework and collagen mass change following the DA-framework, the tissue's growth is completely defined by the myocytes' volumetric changes. These volumetric changes occur through *sarcomerogenesis*, the creation and deposition

of new sarcomere units [15, 51, 25] which can be serial, i.e., in parallel to the main myofiber direction, or parallel, i.e., orthogonal to this direction. As such, it is common practice to assume the generic growth deformation gradient:

$$\mathbf{F}^g = \alpha \mathbf{I} + [\beta - \alpha] \mathbf{f}_0 \otimes \mathbf{f}_0, \quad (40)$$

where  $\alpha$  and  $\beta$  are coefficients that specify the amount of volume change along the longitudinal direction and transverse direction of the myocytes, respectively. Their values define the growth kinematics, and they must ensure that  $\det(\mathbf{F}^g) \equiv \hat{v}$

In this work's case study of cardiac VO, it has been shown that myocytes mainly add sarcomeres in series, leading to an increased length-to-width ratio [51, 20]. As such, we set  $\alpha = 1$  and  $\beta = \hat{v}$ , leading to:

$$\mathbf{F}^g = \mathbf{I} + [\hat{v} - 1] \mathbf{f}_0 \otimes \mathbf{f}_0. \quad (41)$$

#### 4. Multi-constituent G&R in left ventricle volume overload

We implement our G&R framework in an idealized human left ventricle (LV). Figure 2 shows the LV in the unloaded configuration, i.e., the natural configuration that the ventricular chamber would assume in the absence of external forces and internal pressure. The idealized LV domain is represented with a thick-walled prolapsed ellipsoid with variable thickness, as shown on the left with associated dimensions. We distinguish the boundaries associated with the endocardium (inner wall), epicardium (outer wall), and base,  $\Gamma_0^{\text{endo}}$ ,  $\Gamma_0^{\text{epi}}$  and  $\Gamma_0^{\text{base}}$ , respectively. On the right, the local fiber orientation with respect to the tangent plane, i.e., the helix angle, varies transmurally from  $-41^\circ$  in the epicardium to  $-66^\circ$  in the endocardium [52].

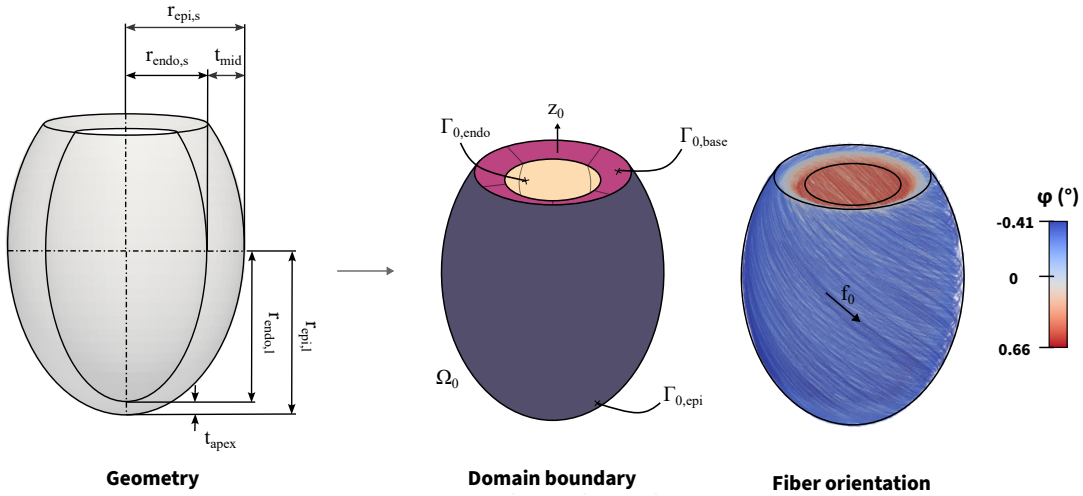


Figure 2: **Schematics of idealized LV model.** The LV geometry is approximately represented by an ellipsoid, whose dimensions are provided (left): the endocardial (outer wall) short and long radius  $r_{\text{endo},s}$  and  $r_{\text{endo},s}$ , and the epicardial (inner wall) short and long radius,  $r_{\text{epi},s}$ ,  $r_{\text{epi},s}$ , and the wall thickness at the mid wall,  $t_{\text{mid}}$  and at the apex,  $t_{\text{apex}}$ . Based on the geometrical parametrization, the surface boundaries are identified (middle), the endocardium  $\Gamma_0^{\text{endo}}$ , the epicardium  $\Gamma_0^{\text{epi}}$  and the basal surface  $\Gamma_0^{\text{base}}$ . Lastly, the fiber orientation is retrieved by analytically computing the fiber direction  $\mathbf{f}_0$  (right) forming an angle with respect to the tangential plane (helix angle) that varies transmurally from  $-41^\circ$  at the epicardium to  $+66^\circ$  at the endocardium.

The mesh is generated using the open-source geometrical modeling and finite element analysis pre- and postprocessor software *pyFormex* [53]. Integration is performed with a  $3 \times 3 \times 3$  Gaussian quadrature rule. The resulting system of equations is solved with a Newton-Raphson iteration scheme using a direct LU

factorization using the Scipy *spsolve* routine, which internally relies on the SuperLU solver [54]. We perform a mesh sensitivity analysis and identify a ventricular mesh of 15,264 linear hexahedral elements, which is found to be a good trade-off between computational time and accuracy.

Table 1 lists the constitutive parameters of our constrained mixture constitutive law defined in Section 3.1. We initialize these parameters leveraging the ex vivo calibration of [55] based on triaxial shear and biaxial tensile testing data of human myocardial tissue [38]. Specifically, we assigned the parameters describing the sheet and sheet-normal behavior in their model to the corresponding collagen parameters in our formulation. For the mean fiber direction, we additively partitioned the load contribution between myocytes and collagen fibers aligned with the fiber direction by adjusting the linear parameters  $a_m$  and  $a_{cf}$ . In the moderate-to-high stretch regime, collagen fibers straighten from their wavy baseline configuration and align with cardiomyocytes, preventing them from overstretching. At VO onset, characterized by elevated myocardial stretches, collagen bears most of the load [56]. Therefore, towards this application, we assume that along the myofiber direction, 30% of the tensile stress is carried by myocytes and 70% by collagen. This assumption could be further refined upon the availability of mechanical testing and histological data in VO. **Appendix A** shows the mixture constitutive model behavior compared to experimental data of [38] in biaxial tensile and triaxial shear mechanical tests.

Given that ex vivo calibration of myocardial tissue tends to lead to overly stiff passive tissue behavior [57], we follow [58] and calibrate two uniform scale factors that multiply, respectively, all linear coefficients ( $a_{\bullet}$ ) and all exponential coefficients ( $b_{\bullet}$ ), by minimizing the mismatch between the end-diastolic pressure-volume curve of our simulation to the Klotz curve [59] from  $V_0$  to EDV at the target EDP. Full details are provided in **Appendix B**.

Parameter		Initial	Rescaled	Unit
<b>Myocytes</b>				
Fiber linear	$a_m$	0.99	0.27	kPa
Fiber exponential	$b_m$	23.7	9.32	–
<b>Collagen</b>				
Fiber linear	$a_{cf}$	2.32	0.67	kPa
Fiber exponential	$b_{cf}$	23.7	9.32	–
Sheet linear	$a_{cs}$	1.41	0.41	kPa
Sheet exponential	$b_{cs}$	20.07	7.89	–
Sheet-normal linear	$a_{cn}$	2.04	0.59	kPa
Sheet-normal exponential	$b_{cn}$	16.98	6.68	–
Shear linear	$a_{cfs}$	0.56	0.17	kPa
Shear exponential	$b_{cfs}$	1.08	0.43	–
<b>Ground matrix</b>				
Isotropic linear	$a_g$	0.95	0.27	kPa
Isotropic exponential	$b_g$	5.45	2.15	–

Table 1: **Material parameters.** Constitutive material parameters, initially optimized for ex-vivo experimental data, and rescaled to match in-vivo pressure-volume response described by the Klotz curve.

To investigate the progression of volume overload-induced LV G&R from a healthy state, we simulate three sequential stages: (i) establish of the mechanobiological equilibrium, (ii) induction of pathological overload by raising the ventricular EDP, and (iii) coupled tissue- and organ-level G&R. Stage (i) yields the end-diastolic configuration, which constitutes the baseline (healthy) condition before any G&R. The ventricle is loaded

with a quasi-static linear ramp in internal pressure from 0 mmHg to the a physiological EDP of 8 mmHg [57] on the endocardial surface  $\Gamma_{0,\text{endo}}$ . Dirichlet boundary conditions are imposed with zero-displacement constraints at the base surface  $\Gamma_{0,\text{base}}$ , while traction-free conditions are prescribed at the epicardial surface  $\Gamma_{0,\text{epi}}$ . The baseline simulation is used to determine  $\bar{\lambda}_{i,\text{hom}}$  in Eq. (38). The end-diastolic isochoric stretch is stored at each Gauss point as the homeostatic value. The pathologic overload step (stage (ii)) is simulated by increasing the EDP to 16 mmHg [60]. Finally, in stage (iii) cardiac G&R is simulated over 130 days, representing the hallmark observed time progression of VO adaptation prior to decompensated heart failure as discussed in [4]. The G&R parameter values used are listed in Table 2. To assess the individual and combined contributions of collagen remodeling and myocyte hypertrophy to left ventricular adaptation, we considered three scenarios: **(C) collagen-only**, where prescribe collagen mass loss with fixed myocyte mass; **(M) myocyte-only**, where we prescribe myocyte-driven growth with no collagen mass change; and **(C+M) combined**, a a physiologically representative scenario integrating both effects. These first two scenarios assess the sensitivity of the multi-constituent framework to the minimum collagen mass ratio and the myocyte growth-rate constant, while the combined case captures their joint influence on left-ventricular structure and function.

Local alterations are quantified by tracking the evolution of the constituent partial density  $\hat{\rho}_i$  and the elastic stretch  $\bar{\lambda}_i$ . Organ-level structural adaptations are assessed by evaluating the end-diastolic cavity volume, reported as (i) the relative change from the initial no-growth state,  $\Delta V_{\text{cav}}(\%)$ , and (ii) the incremental change per G&R cycle,  $\Delta V_{\text{inc}}(\%)$ . To characterize the VO eccentric G&R phenotype, we calculate the three-dimensional sphericity index  $SI$  [61], which quantifies dilation toward a spherical geometry [62] and is defined as:

$$SI = \frac{EDV}{\frac{4}{3}\pi \left(\frac{l}{2}\right)^3}. \quad (42)$$

Lastly, to quantify changes in myocardial tissue stiffness, we evaluate the stress response under biaxial tension with principal stretches applied along the mean-fiber  $\mathbf{f}$  and sheet-normal  $\mathbf{n}$  directions. After each G&R step, we update the constituent densities, rebuild the strain-energy function with the new densities, and load a virtual myocardial tissue specimen with the prescribed stretches.

#### 4.1. Collagen-driven adaptation during ventricular volume overload; (C) collagen-only

We model ECM collagen degradation by prescribing a decay evolution equation for the collagen mass, see Eq. (39), over a growth time interval of nineteen weeks, a typical time frame for animal experiments of VO-induced G&R [12, 13]. Chronically, collagen degradation has been shown to stabilize between weeks 4 and 6, reaching a 30% decrease in volume percentage, with no further changes thereafter [12]. To bound the degradation within this time window, we set the decay parameter  $\tau = 6$  weeks. To assess the impact of collagen loss, we vary the degradation parameter  $\dot{m}_{c,\text{min}} = [0.15, 0.35, 0.55, 0.75]$ , covering scenarios from low degradation up to the maximum mass loss of 85%. We model pure collagen-driven DA by allowing collagen mass to gradually decay, while myocyte mass remains constant. Figure 3 summarizes the evolution of local and global metrics in response to collagen-driven left ventricle adaptation. We illustrate the collagen mass change evolution for each case and the resulting changes occurring at the tissue scale, i.e., changes in myocytes and collagen densities  $\hat{\rho}_m$ ,  $\hat{\rho}_c$ , and elastic stretch along the fiber direction,  $\bar{\lambda}_{ff}$ . Note that myocyte and the collagen fibers aligned with their principal direction experience the stretch  $\bar{\lambda}_m = \bar{\lambda}_{cf} = \bar{\lambda}_{ff}$ .

**Local changes at the tissue scale.** In a pure collagen adaptation scenario, there is no volumetric growth, i.e., the growth tensor reduces to  $\mathbf{F}^g = \mathbf{I}$  and  $\det(\mathbf{F}^g) = \hat{v} = 1$ . Consequently, the change in collagen partial density matches the change in collagen mass, see Figure 3 (top and top-right *tissue level*). In contrast, myocyte partial density remains unchanged, according to Eq. (25), see Figure 3 (left). Locally, the elastic fiber stretch  $\bar{\lambda}_{ff}$  initially rises during the first six weeks, and then stabilizes once collagen degradation reaches its final value.

Category	Parameter	Value	Unit
<b>Geometry</b>	Major endocardial radius	$r_{endo,l}$	mm
	Minor endocardial radius	$r_{endo,s}$	mm
	Apex wall thickness	$t_{apex}$	mm
	Mid wall thickness	$t_{mid}$	mm
	Epicardial fiber helix angle	$\varphi_{epi}$	deg
	Endocardial fiber helix angle	$\varphi_{endo}$	deg
<b>Constitutive model</b>	<b>Myocytes</b>		
	Fiber linear	$a_m$	0.27
	Fiber exponential	$b_m$	9.32
	<b>Collagen</b>		
	Fiber linear	$a_{cf}$	0.67
	Fiber exponential	$b_{cf}$	9.32
	Sheet linear	$a_{cs}$	0.41
	Sheet exponential	$b_{cs}$	7.89
	Sheet-normal linear	$a_{cn}$	0.59
	Sheet-normal exponential	$b_{cn}$	6.68
	Shear linear	$a_{cfs}$	0.17
	Shear exponential	$b_{cfs}$	0.43
<b>Ground matrix</b>			
	Isotropic linear	$a_g$	0.27
	Isotropic exponential	$b_g$	2.15
	Volumetric penalty	$\mu$	150
<b>Boundary conditions</b>	Preload diastolic pressure	$P_{pre}$	mmHg
	Overload diastolic pressure	$P_{over}$	mmHg
<b>Initial volume fractions</b>	Myocyte volume fraction	$\phi_0^m$	0.70
	Collagen volume fraction	$\phi_0^c$	0.026
	Ground matrix volume fraction	$\phi_0^e$	0.274

Table 2: **LV volume overload parameters.** Parameters defining the left ventricle geometry, constitutive model, and boundary conditions. Constituent-specific material parameters for myocytes, collagen, and ground matrix, as well as initial volume fractions, are reported.

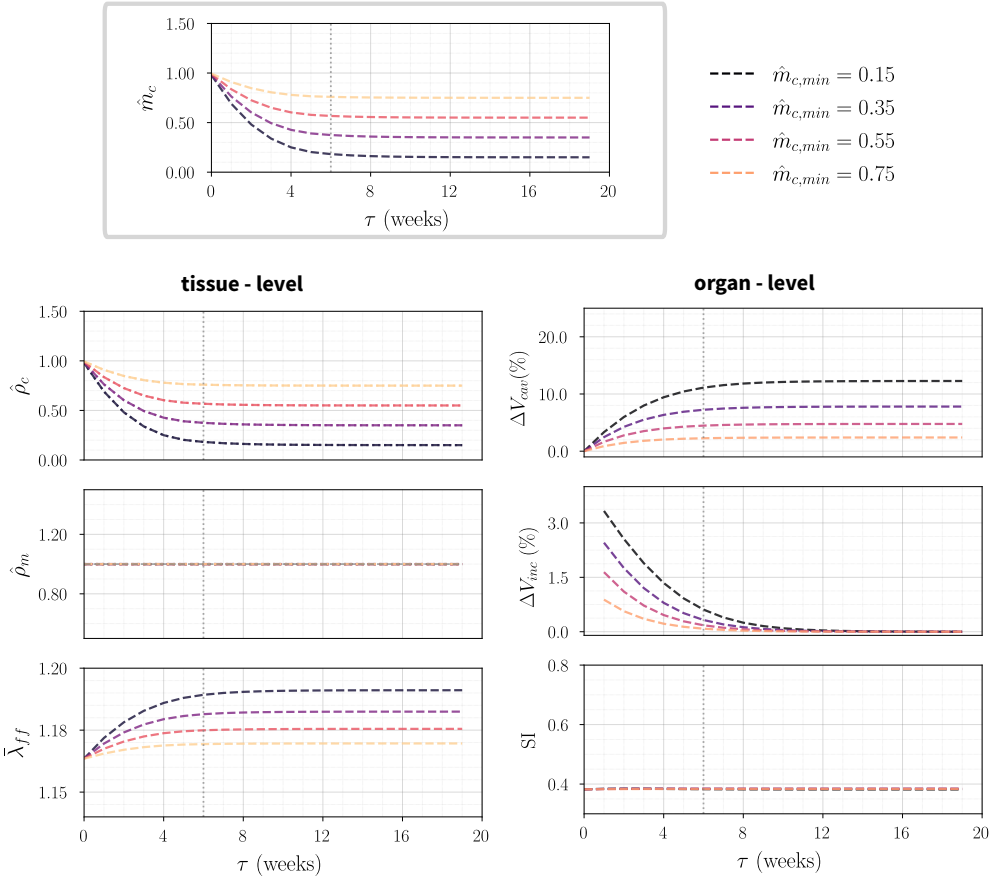


Figure 3: **Collagen mass-driven local and global changes.** G&R changes are quantified for each case over nineteen weeks, where week 0 corresponds to the reference no-grown configuration. On the right, tissue-level changes are represented through the evolution of the collagen partial density  $\hat{\rho}_c$ , the myocyte partial density  $\hat{\rho}_m$ , and the local stretch along the myocyte direction  $\bar{\lambda}_{ff}$ . Global changes reflect alteration in left ventricular cavity volume, quantified through  $\Delta V_{cav}(\%)$ ,  $\Delta V_{inc}(\%)$ , and the SI (left).

**Global changes at the organ scale.** Changes in the microstructure lead to geometrical changes at the organ level, as shown in Figure 3 (right). Globally, an increase in the end-diastolic stretch translates to a higher EDV, see Figure 3 (*organ level* first and second plot). Over nineteen weeks of G&R, LV cavity volume,  $\Delta V_{\text{cav}}$ , increases from 2.4% to 12.3%, corresponding to the limiting cases of 25% and 85% collagen degradation, respectively. No significant changes are observed in the sphericity index for collagen-driven G&R, suggesting that collagen degradation alone, which is prescribed uniformly in all directions, does not induce a change in LV phenotype, with sphericity index SI values remaining around 0.4 throughout G&R, as illustrated in Figure 3 (bottom-right). Following the time course of collagen degradation, most of the changes occur within the first six weeks, with the higher value of the incremental  $\Delta V_{\text{inc}}$  of 3.3% in the first week, for the case of maximum degradation. The resulting LV geometry at the end of G&R is displayed in Figure 3 for each simulated case. Elastic stretches vary transmurally across the LV wall, showing higher values at the endocardial surface, and increase further with greater collagen mass loss, as shown in Figure 4.

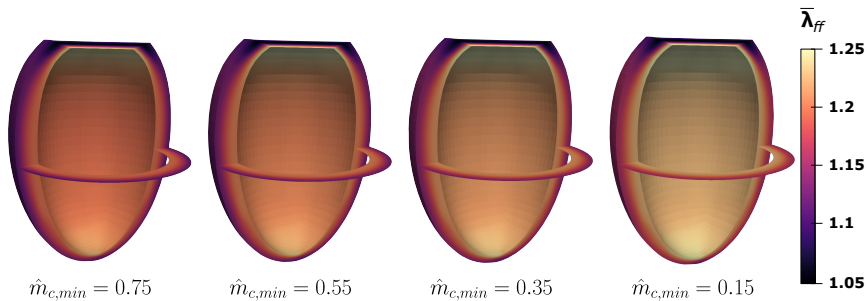


Figure 4: **Elastic stretches.** The spatial distribution of the elastic stretch along the mean fiber direction is shown at week 19, at the end of the simulated growth. Collagen mass loss yields higher elastic stretches, which increase from the LV endocardium to the LV epicardium. Globally, it induces a negligible change in LV phenotype.

**Evolving tissue compliance.** Figure 5 (left) shows the biaxial stretch-stress response along the myofiber and cross-myofiber direction, at the end of week 19. To assess the influence of net collagen degradation on tissue properties, we observe the case corresponding to  $\hat{m}_{c,\min} = 0.35\%$ . Compared to the baseline, the myocardial stiffness decreases in both the myofiber and the cross-myofiber direction, reflected by the lowering of the stress-strain curve. The first weeks display the highest shift, following the rapid degradation of collagen mass, which occurs during the first six weeks. Figure 5 (right) illustrates how collagen degradation alters the load-bearing behavior of myocardial constituents. At baseline, collagen fibers contribute significantly to the passive stiffness in the fiber direction and dominate that in the sheet-normal direction. After 19 weeks of G&R, reduced collagen content leads to a decrease in total stress. This behavior explains the previous finding of increased elastic stretches during growth and, consequently, increased EDV at the organ level.

In summary, our **(C) collagen-only** model shows that collagen mass degradation - predominantly occurring within the first six weeks after VO induction - does not induce significant volumetric change but causes significantly more compliant tissue behavior as the local collagen density decreases.

#### 4.2. Myocyte-driven adaptation during ventricular volume overload; (M) myocyte-only

Myocyte-driven adaptation is modeled through the stretch-dependent law introduced in Eq. (38). In four simulations, we let the growth rate parameter  $\kappa_m$  vary within the range  $\kappa_m = [0.2, 0.3, 0.4, 0.5]$  (week). In contrast to other myocyte-driven G&R models [15, 27], we do not impose an artificial upper limit on myocyte growth. Instead, growth evolves linearly and is triggered when the local elastic stretches along the fiber-direction deviates from its homeostatic value. Figure 6 summarizes the evolution of local and global quantities in response to myocyte-driven left ventricle overload.

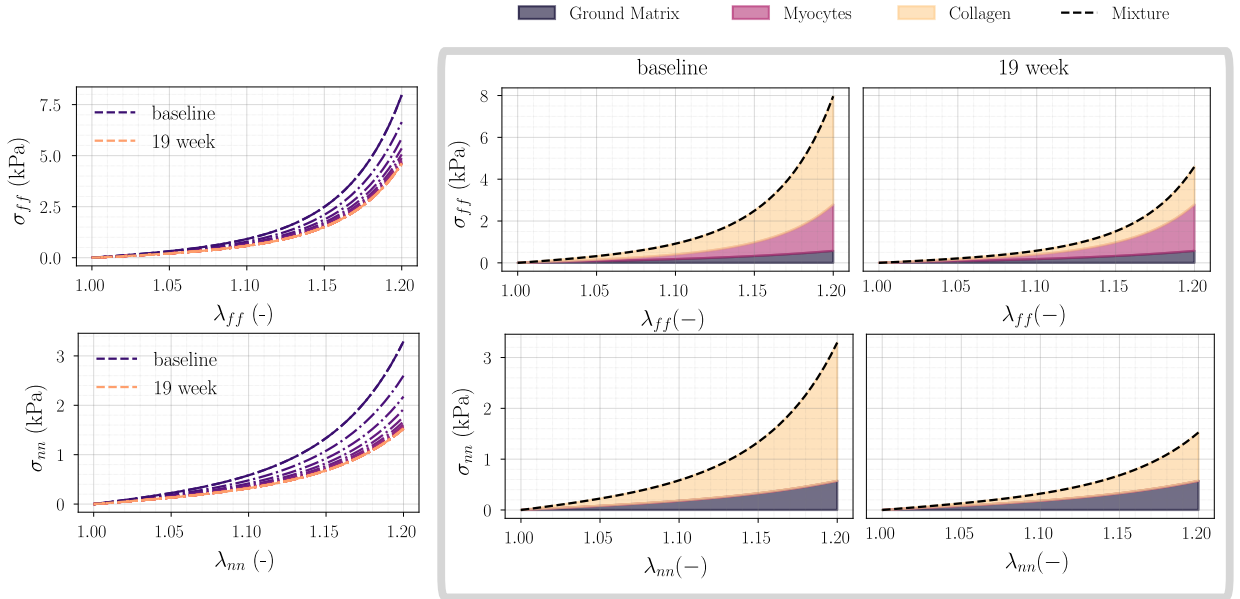


Figure 5: **Biaxial properties during collagen-driven G&R.** The stretch-stress behavior is plotted at the end of each growth cycle. Each curve refers to one G&R week, spanning from the baseline no-growth time (dotted line) to the end of the simulated growth corresponding to week 19. On the right, the contribution of each constituent to tensile stress is displayed at baseline and at week 19.

**Local changes at the tissue scale.** Myocytes respond to volume overload by increasing their mass during the nineteen-week G&R period, reaching 1.11 and 1.22 times their initial value for  $\kappa_m = 0.2$  and  $\kappa_m = 0.5$ , respectively. [13] measured myocyte elongation of 9% and 18% at week 9 and 16, which is in agreement with our results when  $\kappa_m = 0.4$ . Following the VA assumption, local changes in myocyte mass imply, at the kinematic level,  $\mathbf{F}^g \neq \mathbf{I}$  and  $\det(\mathbf{F}^g) = \hat{v} \neq 1$ . Here, the additional volume is accommodated along the principal myofiber direction, as we specify an anisotropic growth deformation gradient, via Eq. (41). At the tissue level, the volumetric change  $\hat{v}$  implies that both myocyte and collagen partial densities vary according to Eq. (25), see Figure 6 (*tissue level* first plot). In particular, collagen partial density decreases as a consequence of myocyte growth in volume. A key distinction from the previous collagen mass-driven case is that the elastic fiber stretch  $\bar{\lambda}_{ff}$  gradually decreases during G&R. According to the kinematic growth theory assumption, myocytes elongate so that the elastic homeostatic stretch is locally retrieved. In other words, without any change in tissue properties, the inelastic growth induced by myocytes progresses until the target stretch is reached at each material point. The higher the growth rate parameter governing myocyte growth, the faster the homeostatic state goes back towards the homeostatic value, see Figure 6 (left).

**Global changes at the organ scale.** Organ-level changes are shown in Figure 6 (right). At the end of week 19, myocyte hypertrophy induces an increase in EDV cavity of 17 % and 27% for the growth rate parameter  $\kappa_m = 0.2$  and  $\kappa_m = 0.5$ , respectively. Similar to the collagen G&R scenario, most of the changes occur before the first ten weeks of G&R. In fact, the mechanical stimulus felt by myocytes is progressively reduced as the deviation from the homeostatic state decreases. The value of  $\Delta V_{inc}$  decreases from 2.4% at week 3 to 0.5% at week 19, for  $\kappa_m = 0.5$ . The geometrical modification induced by myocyte G&R results in the eccentric phenotype, where the LV assumes a more spherical shape [61]. This is reflected by the resulting sphericity  $SI$ , which increases from its original value of 0.38 to a maximum of 0.6 at week 19. Figure 6 (bottom) visualizes the distribution of the mechanical stimulus, the elastic fiber stretch, on the grown configuration at week 19. The most elevated stretches are found in the LV endocardium, with maximum values in proximity to the region of the LV apex.

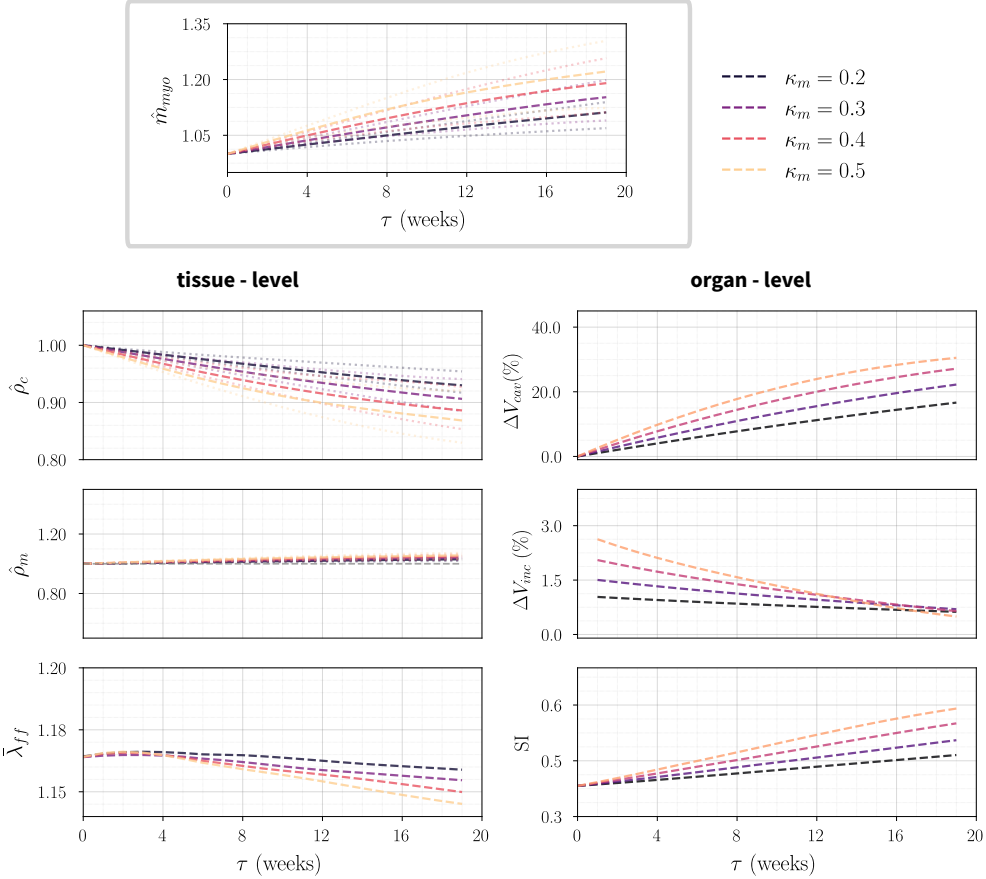


Figure 6: **Myocyte mass-driven local and global changes.** G&R changes are quantified for each case over nineteen weeks, where week 0 corresponds to the reference no-grown configuration. On the right, tissue-level changes are represented through the evolution of the collagen partial density  $\hat{\rho}_c$ , the myocyte partial density  $\hat{\rho}_m$ , and the local stretch along the myocyte direction  $\bar{\lambda}_{ff}$ . Global changes reflect alteration in left ventricular cavity volume, quantified through  $\Delta V_{cav}(\%)$ ,  $\Delta V_{inc}(\%)$ , and the SI (left). Dotted lines denote the interquartile range (25th–75th percentiles).

**Evolving tissue compliance.** The biaxial tensile test, performed at the end of each G&R week, shows almost no change in the passive stress-strain behavior of myocardium during G&R, as shown in Figure 8. Under the VA assumption, myocyte mass change does not directly affect the tissue constitutive response. However, the increase in volume by myocyte hypertrophy lowers the partial density of collagen. Consequently, the biaxial mechanical response exhibits a slight softening in the sheet-normal direction, where collagen is the primary load-bearing constituent, see Figure 7 (right). Similarly, in Figure 7 (right), we observe no significant change in the relative collagen contribution in passive stiffness, besides a slight decrease along the sheet-normal direction.

In summary, our **(M) myocyte-only** model shows that myocytes contribute to left ventricular G&R by increasing their mass in an attempt to bring the elevated stretch induced by VO back to their homeostatic value. At the organ scale, myocyte hypertrophy drives left ventricular enlargement, producing the eccentric phenotype, with almost no changes to tissue mechanical properties.

#### 4.3. Combined collagen and myocyte adaptation during ventricular volume overload; (C+M) combined

In the previous subsections, we isolated the contributions of myocyte and collagen G&R, and carried out a sensitivity analysis of the G&R parameters. Based on these results, we select adequate growth parameters

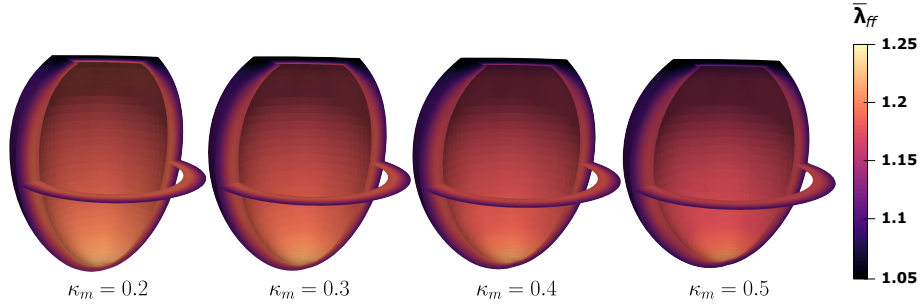


Figure 7: **Elastic stretches.** The spatial distribution of the elastic stretch along the mean fiber direction is shown at week 19, at the end of the simulated growth. Myocyte mass growth lowers elastic stretches in the LV. At the organ scale, it promotes eccentric growth and a more spherical LV shape.

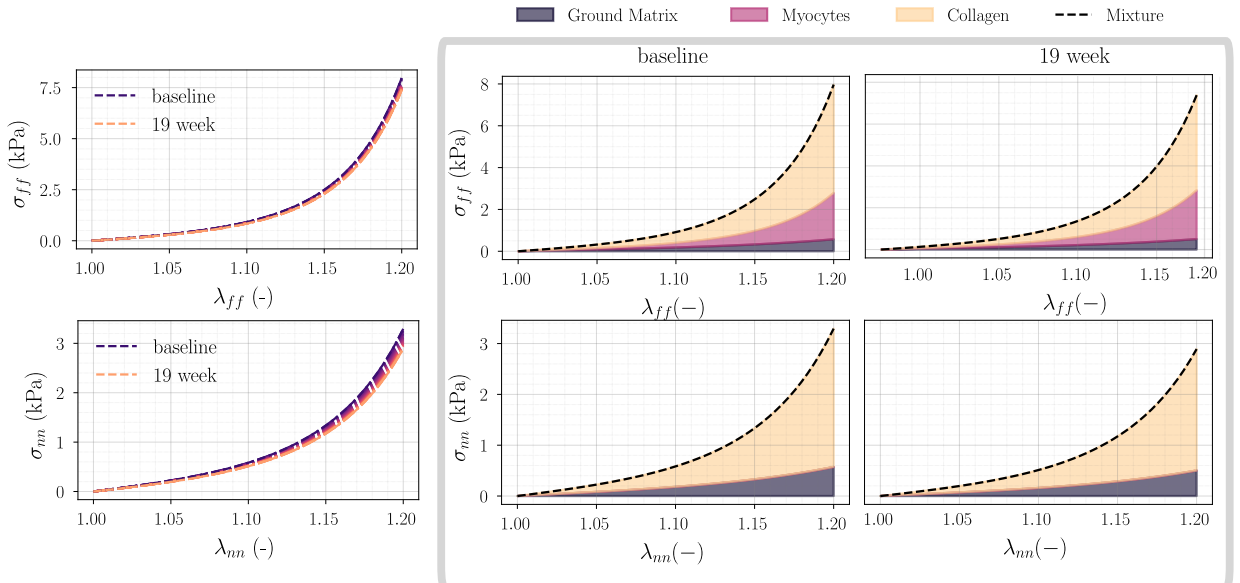


Figure 8: **Biaxial properties during myocytes-driven G&R.** The stretch-stress behavior is plotted at the end of each growth cycle(left). Each curve refers to one G&R week, spanning from the baseline no-growth time (dotted line) to the end of the simulated growth corresponding to week 19. On the right, the contribution of each constituent to tensile stress is displayed at baseline and at week 19.

to reproduce a physiologically relevant case, to study the reciprocal roles of collagen and myocyte adaptation. We set  $\kappa_m = 0.4$ , which in the pure myocyte-driven growth scenario yielded the closest match to the hypertrophy of myocytes measured experimentally [13]. Simultaneously, we prescribe a collagen mass degradation of 30%, i.e., that reaches a minimum value of  $\hat{m}_{c,\min} = 0.7$  at week 5, which is then maintained unaltered for the remaining G&R time points, based on the experimental observation in [13]. In Figure 9, this combined scenario, denoted C+M, along with a pure collagen DA scenario, denoted scenario C, and a pure myocyte VA scenario, denoted M.

**Collagen and myocyte interplay at the tissue scale.** Compared to a pure myocyte elongation case, the presence of 30% collagen degradation, albeit moderate, further enhances myocyte hypertrophy, with myocyte mass increasing from 6.2% and 16% in scenario M to 7.3% and 19% in scenario C+M at weeks 8 and 15 post-VO, respectively, see Figure 9 (top right). In fact, the decrease in collagen mass density during the first six weeks alters the mechanical behavior by increasing tissue compliance and thus end diastolic elastic stretches, as was in the case of the pure collagen case. Since myocyte G&R is mechano-driven, their mass increases in proportion to the deviation from the stretch homeostatic value, which is higher in the presence of collagen degradation (scenario C+M), compared to pure myocyte growth (scenario M). Thus, early collagen degradation not only promotes ventricular dilatation by reducing myocardial stiffness but also further enhances myocyte hypertrophy. Regarding changes in tissue composition, the partial density of collagen decreases in all three scenarios. Figure 10 illustrates the local volume change driven by myocyte and collagen mass changes at weeks 0, 5, 8, 15, 19 post VO onset. After each G&R cycle, individual volume fractions are updated, reflecting changes in the volume occupied by each constituent with respect to the total tissue volume. Figure 11 shows the temporal evolution of the constituents' volume fractions, expressed in terms of median value and interquartile range. Consistent with mass changes in both collagen and myocytes, myocyte volume fraction increases, whereas both collagen and ground matrix fractions decrease throughout the simulated G&R.

**Collagen and myocyte interplay at the organ scale.** Myocyte growth alone (scenario M) results in a 27% increase in LV volume by week 19, whereas collagen degradation alone scenario C produces only a minor dilation, less than 3%. Crucially, when the two mechanisms act together in scenario C+M, the cavity volume increases by 35%, corresponding to an LV volume of 194 ml at week 19. Collagen loss, in fact, by promoting the hypertrophic response of myocytes, favors geometrical and structural changes in LV, which leads ultimately to higher ventricular enlargement. This is also reflected in the G&R phenotype of the LV, as the transition toward a more spherical chamber geometry is further accentuated (with values reaching  $SI = 0.55$  in scenario M compared to  $SI = 0.6$  scenario C+M) when myocyte hypertrophy occurs in the presence of collagen degradation, see Figure 9 (*organ-level* third plot).

In summary, the reciprocal role of collagen degradation and myocyte G&R can be explained mechanistically, such that collagen loss causes a decrease in myocardial compliance, resulting in increased end-diastolic stretches, i.e., a higher mechanical stimulus for myocyte G&R. Globally, this results in a more dilated and spherical LV.

## 5. Discussion

Hearts undergoing VO experience a series of distinct anatomical and functional modifications, which include left ventricular dilatation, decreased radius/wall thickness, and increased sphericity [5, 2, 63]. Such macroscopic changes stem from an intricate cascade of microstructural processes, dominated by myocyte adaptation and collagen remodeling. While myocyte growth has been studied in the literature both numerically and experimentally and is recognized as the dominant cellular event contributing to LV eccentric hypertrophy, [64, 65, 25, 20], the role of collagen remodeling is often overlooked. Recently, experimental studies have emphasized the influence of extracellular collagen G&R, in both early and chronic progression of VO remodeling [10, 66, 13, 12]. These studies suggest that persistent collagen degradation, parallel to myocyte hypertrophy, is a central factor in the progression of VO. Despite its clinical relevance, the

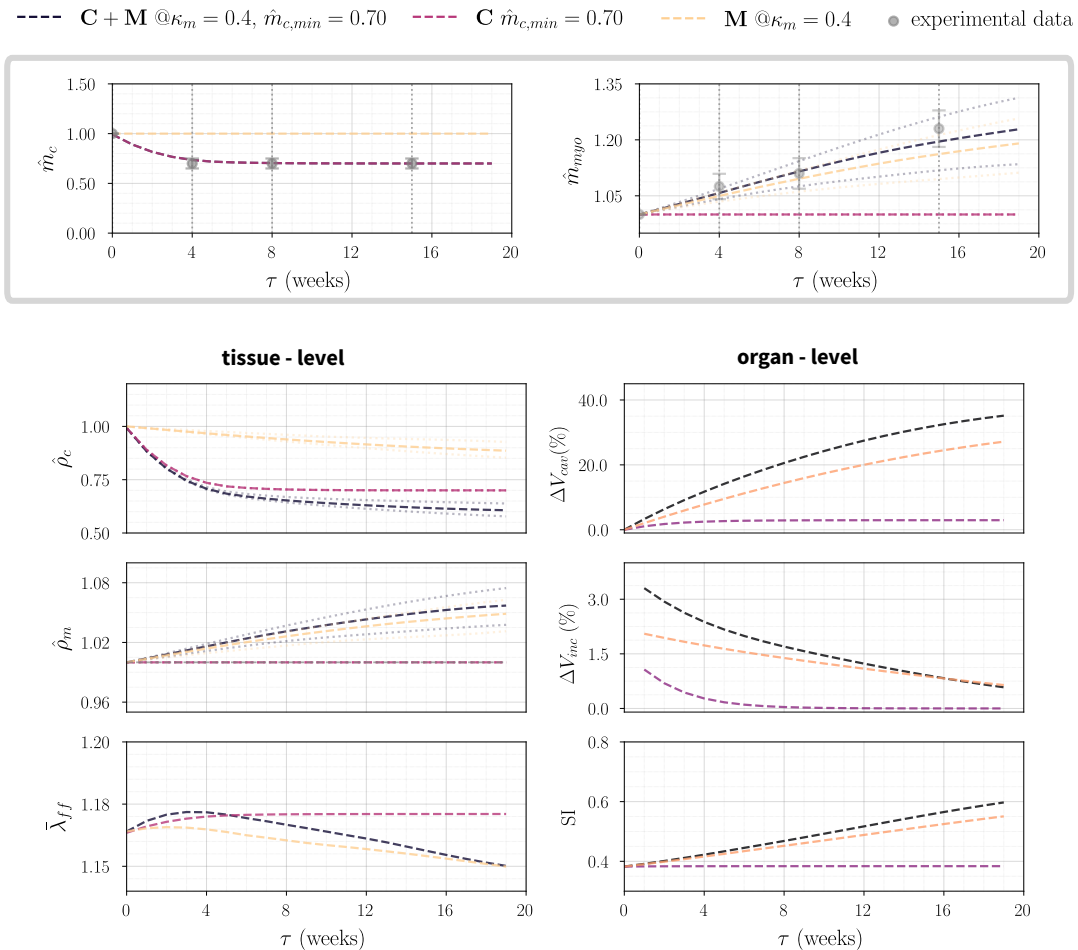


Figure 9: **Collagen and myocyte mass-driven global and local changes.** G&R changes are quantified for each case over nineteen weeks. Constituent's partial densities, local stretch along the myocyte direction are plotted (right). Global changes reflect alteration in left ventricular cavity volume, quantified through  $\Delta V_{\text{cav}}(\%)$ ,  $\Delta V_{\text{inc}}(\%)$ , and the sphericity index. Dotted lines indicate the interquartile range (25th–75th percentiles) and the gray dots mark experimental values for collagen and myocytes mass change from [13].

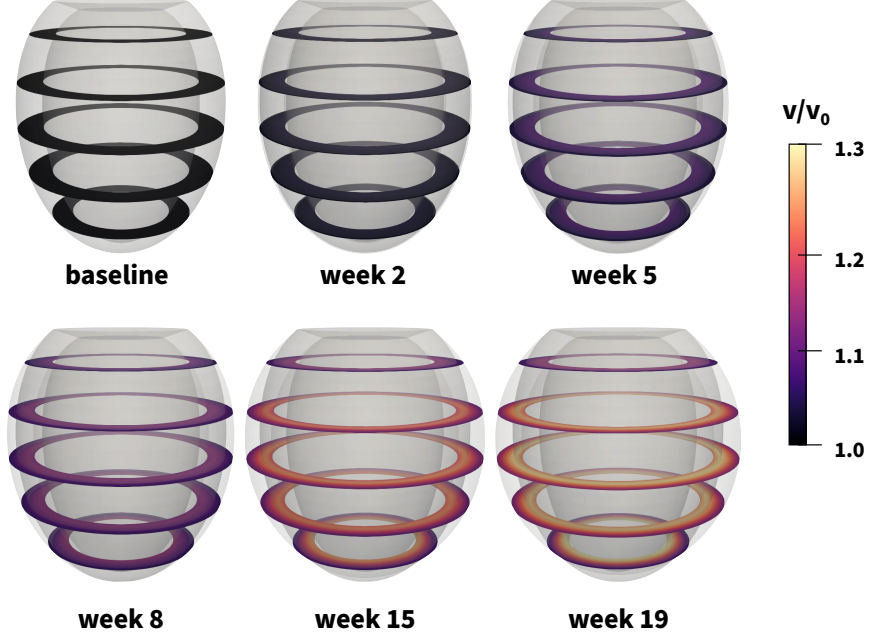


Figure 10: **Collagen and myocyte-driven G&R.** The total tissue volume change is shown at week 0 (baseline) week 5, 8, 15, 19. Additionally, the local evolution of volume fractions is shown for myocardial constituents (myocytes, collagen, ground matrix). Dashed lines denote median values, while dotted lines indicate the interquartile range (25th–75th percentiles).

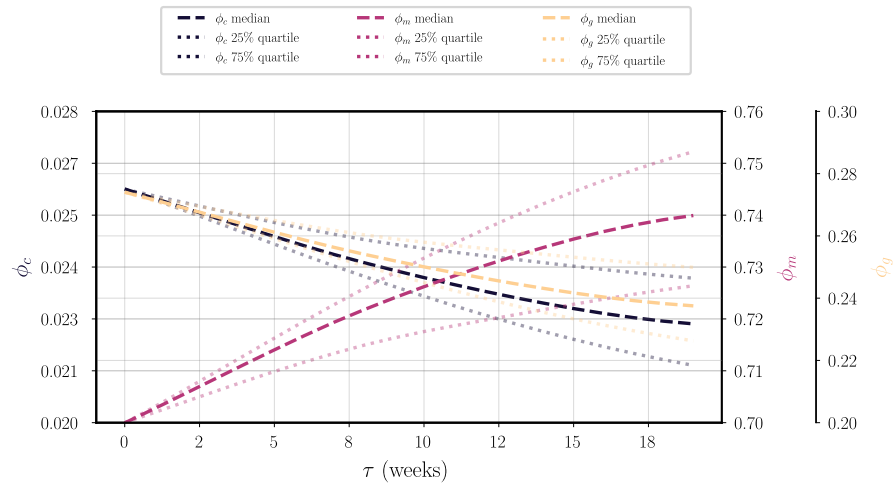


Figure 11: **Collagen and myocyte-driven changes in volume fractions.** The local evolution of volume fractions is shown for myocardial constituents (myocytes, collagen, ground matrix). Dashed lines denote median values, while dotted lines indicate the interquartile range (25th–75th percentiles).

mechanobiological basis of G&R across scales remains largely unclear, and the cause-and-effect relationships governing constituents' interplay are still under investigation.

**Collagen degradation causes myocardial softening in volume overload.** The developed microstructure-informed mechanical framework enables the linking of mass changes in individual myocardial constituents to both organ-scale geometrical changes, such as alterations in left ventricle dimensions and phenotype, and constitutive changes, reflected in myocardial tissue stiffness. The first objective is to discern which of these alterations are predominantly driven by myocyte or collagen G&R (and to what extent), thereby isolating the respective roles of these processes in governing left ventricle adaptation in response to volume overload. When modeling collagen degradation alone, our numerical results indicate that a significant decrease in collagen mass alters myocardial tissue properties by inducing a softening in the strain-strain response during the progression of volume overload. The biaxial-tensile response evaluated at each G&R week shows a progressive decrease in mechanical stiffness compared to the baseline in both fiber and sheet-normal direction, where collagen predominantly contributes to load bearing. As it follows a density-adaptation process, changes in collagen mass do not yield volumetric growth. Locally, this means that elastic stretches accumulate in the tissue without any compensatory inelastic deformation. At the organ level, the loss of load-bearing capacity promotes ventricular dilatation [12]. Similar results were obtained by [43], which linked constitutive changes attributed to collagen mass to LV G&R in myocardial infarction. Interestingly, their findings suggested that collagen fibrosis, i.e., an increase in collagen mass, impairs myocardial compliance and thus yields to diastolic dysfunction, confirming reported experimental results [67, 68]. Notably, their image-based framework models fibrosis at the constitutive level by modifying the strain energy function through weighting parameters that directly represent variations in collagen fiber mass and thickness. These parameters remain constant over time and are identified to reproduce single-time-point ex vivo mechanical tests of infarcted tissue. By contrast, our G&R framework inherently captures myocardial adaptation by allowing the strain-energy function to evolve in time through constituent partial densities. In doing so, it naturally captures the temporal dynamics of the G&R processes, including their mutual influence on other constituents and on volumetric growth. In the context of cardiovascular tissue, a recent work by [48] developed an energy-based model for the evolution of collagen density and collagen reorientation in cardiovascular tissue during maturation, where strain energy functions depend explicitly on collagen fiber density. Similarly to our formulation, [48] coupled the constitutive description with volumetric growth through a stress-driven homeostatic surface approach. However, in their model only collagen density is set to change, and other constituent densities remain constant. Here, the individual changes in mass and volume of all constituents mutually influence their relative amounts in the tissue through partial mass densities, which results in the redistribution of load among the structural constituents.

**Myocyte hypertrophy dictates eccentric phenotype in volume overload.** When simulating purely myocyte mass-driven G&R, myocyte hypertrophy produces a marked increase in the LV cavity, reaching 27% above its baseline dimension in response to a 22% increase in myocyte mass. The inelastic growth induced by myocytes acts to restore the elastic stretch toward its homeostatic value. Our G&R model captures characteristic features of myocyte-driven eccentric growth in the left ventricle: sarcomerogenesis and fiber-aligned myocyte elongation promote chamber dilatation with added volume depositing along the parallel direction of myocytes [69, 19, 20]. The distribution and magnitude range of myofiber stretch predicted by our model (Figure 6, *bottom*) are consistent with previous findings [17, 20], which reported that hypertrophy initiates in the endocardium, where higher elastic stretches on average are found, and progresses towards the epicardium. Our numerical results show a progressive transition of the LV from an elliptical to a more spherical shape, with higher values of the sphericity index *SI* associated with increased myocyte growth. A similar trend was reported by [19], who qualitatively observed increased sphericity in their eccentric G&R simulations. Under the volume-adaptation assumption, myocyte hypertrophy increases tissue volume, which indirectly marginally alters the material properties, i.e., a slight tissue softening, as it reduces collagen partial densities.

**Collagen role is key in both myocyte hypertrophy progression and LV dilatation.** The relevance of the proposed framework becomes evident when aiming to represent a physiologically realistic scenario,

in which organ-level adaptation does not arise from a single process—such as myocyte hypertrophy or collagen degradation—but rather emerges from the interplay between the G&R pathways of the individual constituents. Our model captures both structural and functional ventricular changes resulting from the concurrent influence of alterations in collagen density and myocyte hypertrophy under volume overload. In the presence of both myocyte hypertrophy and collagen degradation, the reduction in collagen mass density increases tissue compliance and end-diastolic stretch, thereby amplifying the mechano-driven myocyte growth response. As a result, myocyte mass increases more compared to the pure hypertrophy case. Coherently, at the organ-level, myocyte hypertrophy alone drives substantial dilation. However, when combined with collagen mass decrease, these processes produce a synergistic effect that results in a larger increase in the cavity volume and accentuated eccentric remodeling. Besides the present work, the microstructural-functional relationship in volume-overloaded hearts has been explored through a computational approach only by [27]. In this study, the authors coupled a constitutive mixture model to kinematic growth within an evolving reference configuration approach. In their study, the constitutive model explicitly accounted for myocardial tissue constituents in the strain energy function, weighted by relative volume fractions. However, in their G&R scenarios, the evolution laws rely on a single growth multiplier which is either (i) applied uniformly to both collagen and myocytes, or (ii) applied only to myocytes. As a result, their model suggests that collagen either increases in volume fraction, leading to a progressively stiffer stress-strain response, or exhibits only minimal decreases in volume fraction as a secondary effect of myocyte growth. These outcomes may not capture the dominant processes manifesting at both micro- and organ-scales. In contrast, our framework assigns distinct temporal dynamics to each constituent’s G&R process and prescribes growth type (mass increase or decrease) for each constituent, based on experimental observations. This distinction allows the model to differentiate between structural changes driven by cardiomyocyte elongation and those resulting from extracellular collagen degradation.

**G&R model predictions align with experimental evidence linking collagen degradation to ventricular dilatation.** Collectively, our results demonstrate that although myocyte mass growth is the predominant driver of ventricular dilatation at the organ level, collagen degradation not only accommodates dilatation but also promotes further myocyte hypertrophy. Experimentally, rodent and large-animal models suggest that interstitial collagen loss exacerbates myocyte elongation VO, irrespective of the mode of induction, e.g., aortocaval fistula and mitral regurgitation [70, 66, 13, 12]. In their work, [13] combined LV chamber, cardiomyocyte, and interstitial collagen analyses to assess myocardial changes in aortocaval fistula-induced volume overload. They quantified chronic collagen degradation occurring in the first 5 weeks of 30% loss and measured that volume overload induced a myocyte elongation of 9% and 18% at the 8- and 15-week after induction of volume overload. Furthermore, they demonstrated that early collagen degradation, occurring within the first weeks post VO, is the primary G&R mechanism for ventricular dilatation at an early stage, while myocyte adaptation is secondary. Our results are in good agreement with the chronic myocyte and collagen mass changes reported in the aforementioned study. Notably, [13] reported an acute significant dilatation within the first week - 20% change in end-systolic dimension- attributed solely to collagen degradation. Our model instead predicts that chronic collagen degradation contributes little to ventricular dilatation. However, our simulations neglect the acute collagen decrease of 75% that occurs immediately after the onset of volume overload—within the first days—and instead focus on chronic adaptation over weeks. This explains why, compared to their findings, we observe reduced end-diastolic cavity volumes during the early weeks. To date, no longitudinal studies have examined the relationship between myocyte and collagen sub-processes induced by VO in humans. Recently, [63] performed cardiac magnetic resonance in a cohort of 55 patients, complemented by biopsies obtained during mitral valve surgery. Their findings align with animal studies, confirming that loss of endomysial collagen is a root cause of increased passive compliance and ventricular sphericity. With these observations, we emphasize the need for longitudinal investigations that integrate histological and imaging techniques to quantify both collagen and myocyte mass changes and to assess their contributions to acute and chronic alterations in VO [51, 20].

**Outlook.** Building on our current framework, which captures the interplay between collagen density and myocyte volume changes during the early compensation stages of VO, we foresee relevant future avenues to render our G&R framework more mechanistic in nature. First, our current multi-constituent material

model is calibrated on healthy human myocardial test data [38]. As detailed ex-vivo testing data for diseased tissue remains lacking, there is a strong field-wide need for more in-depth explorations of the intrinsic microstructural organization and functional behavior of diseased myocardial tissue. Such data could further inform an extended material model that incorporates richer microstructural features, including separate endomysial and perimysial collagen and changing fiber thickness contributions [71, 72, 73, 74]. Second, while most VO G&R theories focus on passive stimuli to drive the intrinsic evolution laws, multi-constituent changes are likely to impact the tissue's active response. Therefore, we deem it worthwhile to explore the extension of our framework with active stress laws [75, 76] to rigorously quantify the impact that structural tissue changes have on the cardiac function throughout the full cardiac cycle. Finally, while this study demonstrated the utility of phenomenological collagen decay kinetics, such a simplification omits the biochemical cascades that regulate collagen turnover and myocyte hypertrophy. Developing a multi-constituent G&R model regulated by mechanical cues and biochemical factors, in which we further couple mass rate equations to specific signaling pathways, e.g., fibrogenic proteins and MMPs–TIMPs cascades [50, 32], would enhance the chemo–mechano–biological fidelity of our framework.

## 6. Conclusions

This study presents a multiscale mechanical framework that integrates G&R theory within a multi-constituent formulation to relate alterations in myocardial tissue constituents to geometric and functional changes at the organ level. We quantify the individual and combined contributions of myocyte and collagen processes to changes in end-diastolic volume, growth phenotype, and material properties under VO. Our results highlight the significant role of collagen G&R in not only impairing diastolic function directly but also further accelerating myocyte hypertrophy. Finally, incorporating an integrated framework within realistic cardiac geometries and accounting for active mechanical contributions would enable detailed investigation of the coupled mechanical, biochemical, and structural processes governing G&R across scales, extending the analysis beyond isolated pathways to a level of complexity that remains to date inaccessible to experimental approaches.

## Acknowledgments

M. Peirlinck acknowledges the support from the European Research Council within the European Union's Horizon Europe research and innovation program (VITAL - Grant No. 101136728). We thank F. Gijzen for many valuable discussions, and A. Kewley for his insightful input and technical ingenuity.

## Appendix A - Ex-vivo passive behavior

The initial constitutive parameters were adapted from [55]. Here, these discovered parameters achieve the best fit of the Holzapfel model [37] to experimental ex-vivo biaxial and shear data. In this study, the parameters are further adapted by redistributing the load between collagen fibers oriented parallel to the myocytes and the myocytes themselves. Figure 12 shows the resulting stress responses for biaxial and triaxial shear tests along with the original experimental data.

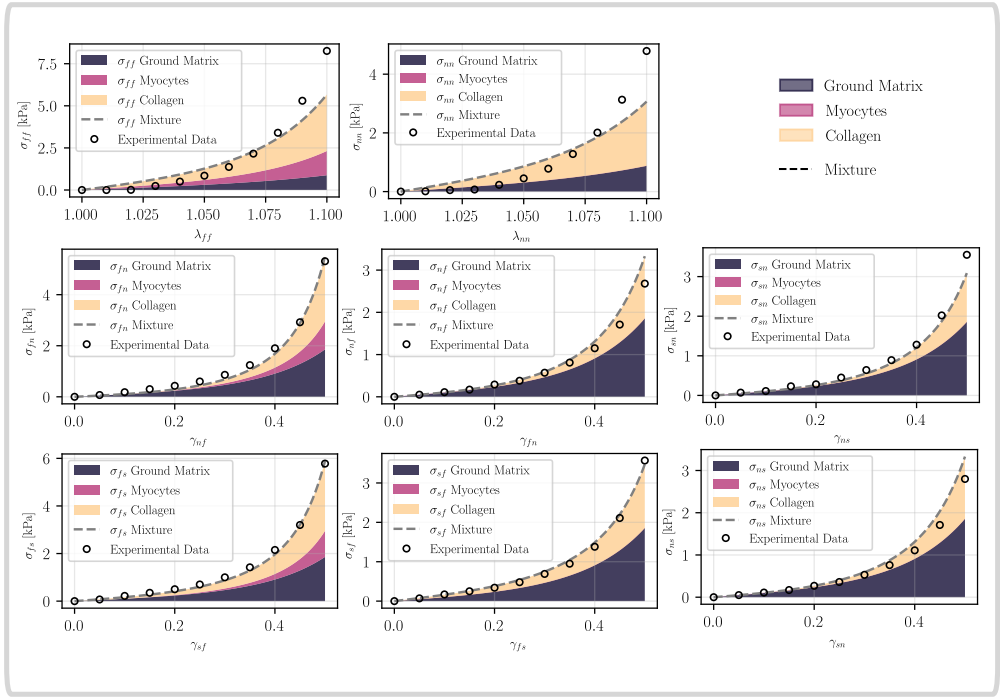


Figure 12: **Ex-vivo biaxial and shear behavior of the cardiac mixture.** The initial constitutive parameters of the cardiac mixture are adapted from [77] such that the best fitting to ex-vivo experimental data is achieved when optimizing for biaxial and triaxial shear data simultaneously. The contribution of each constituent in bearing the passive loading is displayed in terms of constituent-specific Cauchy stress (filled-colored plot regions) as well as the total stress of the mixture (dotted line). The discrete experimental data points are denoted with circles.

## Appendix B - In-vivo parameter optimization

The constitutive parameters in Eq. (11) were rescaled to reproduce a passive physiological response consistent with the in-vivo end-diastolic pressure-volume relationship (EDPVR), as discussed in [58]. Adopting initial parameter values from [77], we adjusted them to distribute the stress contribution along the principal fiber direction between the myocytes and the collagen fibers aligned with the long axis of the myocardium. The linear and exponential terms in the constitutive model were uniformly scaled by factors A and B, optimized to minimize the error between the simulated diastolic pressure-volume response and the analytical Klotz curve [59].

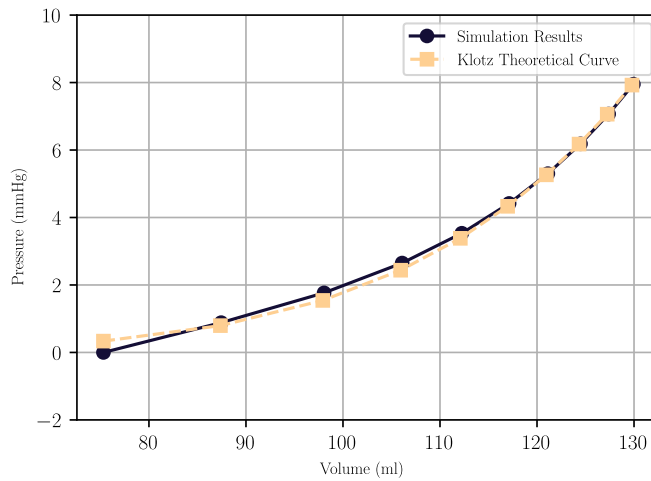


Figure 13: **In-vivo parameter optimization results.** The constitutive parameters of the mixture model are re-scaled by minimizing the relative error between the simulated end diastolic pressure-volume (EDPVR) curve and the theoretical Klotz curve (in ochre). The optimization led to a final simulated EDPVR (in dark purple) displaying a deviation of 0.23 from the analytical Klotz curve.

## Appendix C - Second Piola-Kirchhoff stress and elasticity tensor

Incorporating the myocardial mixture into the finite element framework requires deriving the second volumetric and isochoric Piola-Kirchhoff stresses as outlined in Eq.(14) and (15), along with their derivatives with respect to the right Cauchy-Green tensor  $\mathbf{C}^e$ , the volumetric and isochoric elasticity tensors (17), (18). The volumetric stress can be further expanded into the following:

$$\begin{aligned}\mathbf{S}_{\text{vol}} &= 2 \frac{\partial \psi_{\text{vol}}(J^e)}{\partial \mathbf{C}^e} = 2 \frac{\partial \psi_{\text{vol}}(J^e)}{\partial J^e} : \frac{\partial J^e}{\partial \mathbf{C}^e} = J^e p \mathbf{C}^{e-1} \\ &= J^e \mu (J^e - 1) \mathbf{C}^{e-1}.\end{aligned}$$

Here, we calculate the hydrostatic pressure from the constitutive relation in Eq. (12),  $p = d\psi_{\text{vol}}/dJ^e = \mu(J^e - 1)$ . Taking the derivative of  $\mathbf{S}_{\text{vol}}$  with respect to  $\mathbf{C}^e$ , we can further expand (17) and retrieve:

$$\begin{aligned}\mathbb{C}_{\text{vol}} &= 2 \frac{\partial \mathbf{S}_{\text{vol}}}{\partial \mathbf{C}^e} = 2 \frac{\partial (J^e p \mathbf{C}^{e-1})}{\partial \mathbf{C}^e} \\ &= 2 \mathbf{C}^{e-1} \otimes \left( p \frac{\partial J^e}{\partial \mathbf{C}^e} + J^e \frac{\partial p}{\partial \mathbf{C}^e} \right) + 2 J^e p \frac{\partial \mathbf{C}^{e-1}}{\partial \mathbf{C}^e} \\ &= J^e \tilde{p} (\mathbf{C}^{e-1} \otimes \mathbf{C}^{e-1}) - 2 J^e p (\mathbf{C}^{e-1} \odot \mathbf{C}^{e-1}),\end{aligned}$$

where for convenience we introduced the symbols  $\odot$  to refer to the tensor product according to the rule  $-(\mathbf{C}^{e-1} \odot \mathbf{C}^{e-1})_{ABCD} = -\frac{1}{2}(C_{AC}^{e-1} C_{BD}^{e-1} + C_{AD}^{e-1} C_{BC}^{e-1})$ . The scalar function  $\tilde{p} = p + J(dp/dJ)$  is introduced, and  $p$  as defined above.

By integrating the microstructural constituents' description, Eq. (34), into Eq. (11) and Eq. (13), we can expand the derivatives and retrieve for a generic constituent's strain energy function  $\psi_i$ :

$$\begin{aligned}\mathbf{S}_{\text{iso},i} &= 2\hat{\rho}_i \frac{\partial \bar{\psi}_i(\bar{\mathbf{C}})}{\partial \mathbf{C}^e} = 2\hat{\rho}_i \frac{\partial \bar{\psi}_i(\bar{\mathbf{C}})}{\partial \bar{\mathbf{C}}} : \frac{\partial \bar{\mathbf{C}}}{\partial \mathbf{C}^e} \\ &= 2\hat{\rho}_i \frac{\partial \bar{\psi}_i(\bar{\mathbf{C}})}{\partial \bar{\mathbf{C}}} : \frac{\partial J^{e-2/3} \mathbf{C}^e}{\partial \mathbf{C}^e} \\ &= 2\hat{\rho}_i \frac{\partial \bar{\psi}_i(\bar{\mathbf{C}})}{\partial \bar{\mathbf{C}}} : \left( J^{e-2/3} \frac{\partial \mathbf{C}^e}{\partial \mathbf{C}^e} + \mathbf{C}^e \otimes \frac{\partial J^{e-2/3}}{\partial \mathbf{C}^e} \right) \\ &= 2\hat{\rho}_i \frac{\partial \bar{\psi}_i(\bar{\mathbf{C}})}{\partial \bar{\mathbf{C}}} : J^{e-2/3} \left( \mathbb{I} - \frac{1}{3} \mathbf{C}^e \otimes \mathbf{C}^{e-1} \right) \\ &= \bar{\mathbf{S}}_i : J^{e-2/3} \mathbb{P}^t = J^{e-2/3} \mathbb{P} : \bar{\mathbf{S}}_i \\ &= J^{e-2/3} \text{Dev}(\bar{\mathbf{S}}_i),\end{aligned}$$

where we have used the definition of the projection tensor  $\mathbb{P} = \mathbb{I} - \frac{1}{3} \mathbf{C}^{e-1} \otimes \mathbf{C}^e$  and the deviatoric projection operator  $\text{Dev}(\bullet) = (\bullet) - (1/3)[(\bullet) : \mathbf{C}^e] \mathbf{C}^{e-1}$ , according to [34]. Therefore, for each constituent, it is essential to provide the fictitious stress, defined as  $\bar{\mathbf{S}}_i = 2\hat{\rho}_i \partial \bar{\psi}_i / \partial \bar{\mathbf{C}}$ , which can be readily computed.

### Ground matrix

We specified the ground matrix strain energy function in Eq. (37). The second Piola-Kirchhoff stress takes the following expression:

$$\begin{aligned}\mathbf{S}_{\text{iso},g} &= 2\hat{\rho}_g \frac{\partial \bar{\psi}_g(\bar{I}_1)}{\partial \mathbf{C}^e} = J^{e-2/3} \text{Dev}(\bar{\mathbf{S}}_g) \\ &= 2\hat{\rho}_g J^{e-2/3} \text{Dev} \left( \frac{\partial \bar{\psi}_g(\bar{I}_1)}{\partial \bar{I}_1} \frac{\partial \bar{I}_1}{\partial \bar{\mathbf{C}}} \right) \\ &= 2\hat{\rho}_g J^{e-2/3} \gamma_1 \text{Dev}(\mathbf{I}),\end{aligned}$$

where  $\gamma_1 = \partial\bar{\psi}_1/\partial\bar{I}_1 = \frac{a_g}{2}\exp[b_g(\bar{I}_1 - 3)]$ , and  $\partial\bar{I}_1/\partial\bar{\mathbf{C}} = \mathbf{I}$ .

We further expand the derivatives in Eq. (18) and find for the ground matrix constituent:

$$\begin{aligned}\mathbb{C}_{\text{iso, g}} &= 2 \frac{\partial \mathbf{S}_{\text{iso},g}}{\partial \mathbf{C}^e} = 4\hat{\rho}_g \frac{\partial^2 \bar{\psi}_g(\bar{\mathbf{C}})}{\partial \mathbf{C}^e \partial \mathbf{C}^e} \\ &= 4\hat{\rho}_g \frac{\partial}{\partial \mathbf{C}^e} \left( \gamma_1 \frac{\partial \bar{\psi}_g(\bar{I}_1)}{\partial \mathbf{C}^e} \right) \\ &= 4\hat{\rho}_g \left( \gamma_{11} \frac{\partial \bar{I}_1}{\partial \mathbf{C}^e} \otimes \frac{\partial \bar{I}_1}{\partial \mathbf{C}^e} + \gamma_1 \frac{\partial^2 \bar{I}_1}{\partial \mathbf{C}^e \partial \mathbf{C}^e} \right) \\ &= 4\hat{\rho}_g J^{-4/3} \text{Dev} \mathbf{I} \otimes \text{Dev} \mathbf{I} \\ &\quad - 4\hat{\rho}_g J^{-2/3} \gamma_1 \left( \mathbf{C}^{e-1} \otimes \text{Dev} \mathbf{I} + \text{Dev} \mathbf{I} \otimes \mathbf{C}^{e-1} - \bar{I}_1 \tilde{\mathbb{P}} \right),\end{aligned}$$

where we have added the definition  $\gamma_{11} = \partial\bar{\psi}_g/\partial\bar{I}_1\bar{I}_1 = \frac{a_g b_g}{2}\exp[b_g(\bar{I}_1 - 3)]$ , and introduced the modified projection tensor  $\tilde{\mathbb{P}} = \mathbf{C}^{-1} \odot \mathbf{C}^{-1} - \frac{1}{3}\mathbf{C}^{-1} \otimes \mathbf{C}^{-1}$ .

### Collagen fibers

Collagen fibers isochoric contribution to the elastic stress includes the tension-related terms and the shear term, Eq.(36). We can, thus, compute it as:

$$\begin{aligned}\mathbf{S}_{\text{iso},c} &= 2\hat{\rho}_c \frac{\partial \bar{\psi}_c(\bar{I}_{4i}, \bar{I}_{8,fs})}{\partial \mathbf{C}^e} = J^{e-2/3} \text{Dev}(\bar{\mathbf{S}}_c) \\ &= 2\hat{\rho}_c J^{e-2/3} \text{Dev} \left( \sum_{i \in \{f,s,n\}} \frac{\partial \bar{\psi}_{c,i}(\bar{I}_{4i})}{\partial \bar{I}_{4i}} \frac{\partial \bar{I}_{4i}}{\partial \bar{\mathbf{C}}} \right) \\ &\quad + 2\hat{\rho}_c J^{e-2/3} \text{Dev} \left( \frac{\partial \bar{\psi}_{c,fs}(\bar{I}_{8,fs})}{\partial \bar{I}_{8,fs}} \frac{\partial \bar{I}_{8,fs}}{\partial \bar{\mathbf{C}}} \right) \\ &= \hat{\rho}_c J^{e-2/3} \sum_{i \in \{f,s,n\}} \gamma_{4i} \text{Dev}(\mathbf{A}_{0,i}) + \hat{\rho}_c J^{e-2/3} \gamma_8 \text{Dev}(\mathbf{S}_{0,1}),\end{aligned}$$

where  $\gamma_{4i} = \partial\bar{\psi}_{c,i}/\partial\bar{I}_{4i} = a_{c,i}(\bar{I}_{4i} - 1)\exp[b_{c,i}(\bar{I}_{4i} - 1)^2]$  and  $\gamma_8 = \partial\bar{\psi}_c/\partial\bar{I}_{8,fs} = a_{fs}(\bar{I}_{8,fs})\exp[b_{fs}\bar{I}_{8,fs}^2]$ , defined for the tensile and shear terms respectively. We have also used  $\partial\bar{I}_{4i}/\partial\bar{\mathbf{C}} = \mathbf{A}_{0,i}$ . The structural direction tensor  $\mathbf{A}_{0,i}$  in the undeformed configuration is specified in each direction, i.e.,  $\mathbf{A}_{0,f} = \mathbf{f}_0 \otimes \mathbf{f}_0$ ,  $\mathbf{A}_{0,s} = \mathbf{s}_0 \otimes \mathbf{s}_0$  and  $\mathbf{A}_{0,n} = \mathbf{n}_0 \otimes \mathbf{n}_0$ . Finally, we computed  $\partial\bar{I}_{8,fs}/\partial\bar{\mathbf{C}} = \mathbf{S}_{0,i}$ , thus introducing a structural tensor in the  $fs$ -plane,  $\mathbf{S}_0 = 1/2(\mathbf{f}_0 \otimes \mathbf{s}_0 + \mathbf{s}_0 \otimes \mathbf{f}_0)$ . Lastly, it was convenient to use the notation  $\bar{\psi}_{c,i}(\bar{I}_{4,i}) = \frac{a_{c,i}}{2b_{c,i}} \{ \exp[b_{c,i}(\bar{I}_{4,i} - 1)^2] - 1 \}$  and  $\bar{\psi}_{c,fs}(\bar{I}_{8,fs}) = \frac{a_{c,fs}}{2b_{c,fs}} \{ \exp[b_{c,fs}(\bar{I}_{8,fs})^2] - 1 \}$  to indicate the strain energy terms associated to tension and shear contributions, respectively.

The isochoric contribution of the elasticity tensor related to collagen fibers can be expressed as:

$$\begin{aligned}
\mathbb{C}_{\text{iso, c}} &= 2 \frac{\partial \mathbf{S}_{\text{iso, c}}}{\partial \mathbf{C}^e} = 4 \hat{\rho}_c \frac{\partial^2 \bar{\psi}_c(\bar{\mathbf{C}})}{\partial \mathbf{C}^e \partial \mathbf{C}^e} \\
&= 4 \hat{\rho}_c \frac{\partial}{\partial \mathbf{C}^e} \left( \sum_{i \in \{f, s, n\}} \gamma_{4,i} \frac{\partial \bar{\psi}_{c,i}(\bar{I}_{4,i})}{\partial \mathbf{C}^e} + \gamma_8 \frac{\partial \bar{\psi}_{cfs}(\bar{I}_{8,fs})}{\partial \mathbf{C}^e} \right) \\
&= 4 \hat{\rho}_c \left( \sum_{i \in \{f, s, n\}} \gamma_{44,i} \frac{\partial \bar{I}_{4,i}}{\partial \mathbf{C}^e} \otimes \frac{\partial \bar{I}_{4,i}}{\partial \mathbf{C}^e} + \gamma_{4,i} \frac{\partial^2 \bar{I}_{4,i}}{\partial \mathbf{C}^e \partial \mathbf{C}^e} \right) \\
&\quad + 4 \hat{\rho}_c \left( \gamma_{88} \frac{\partial \bar{I}_{8,fs}}{\partial \mathbf{C}^e} \otimes \frac{\partial \bar{I}_{8,fs}}{\partial \mathbf{C}^e} + \gamma_8 \frac{\partial^2 \bar{I}_{8,fs}}{\partial \mathbf{C}^e \partial \mathbf{C}^e} \right) \\
&= 4 \hat{\rho}_c J^{-4/3} \sum_{i \in \{f, s, n\}} \gamma_{44,i} \text{Dev} \mathbf{A}_{0,i} \otimes \text{Dev} \mathbf{A}_{0,i} \\
&\quad - 4 \hat{\rho}_c J^{-2/3} \sum_{i \in \{f, s, n\}} \gamma_{4,i} \left( \mathbf{C}^{e-1} \otimes \text{Dev} \mathbf{A}_{0,i} + \text{Dev} \mathbf{A}_{0,i} \otimes \mathbf{C}^{e-1} - \bar{I}_{4,i} \tilde{\mathbb{P}} \right) \\
&\quad + 4 \hat{\rho}_c J^{-4/3} \gamma_{88} \text{Dev} \mathbf{S}_0 \otimes \text{Dev} \mathbf{S}_0 \\
&\quad - 4 \hat{\rho}_c J^{-2/3} \gamma_8 \left( \mathbf{C}^{e-1} \otimes \text{Dev} \mathbf{S}_0 + \text{Dev} \mathbf{S}_0 \otimes \mathbf{C}^{e-1} - \bar{I}_8 \tilde{\mathbb{P}} \right),
\end{aligned}$$

where  $\gamma_{44,i} = \partial \bar{\psi}_{c,i}^2 / \partial \bar{I}_{4,i} \partial \bar{I}_{4,i} = a_{c,i} \exp[b_{c,i}(\bar{I}_{4,i} - 1)^2] [1 + 2b_{c,i}(\bar{I}_{4,i} - 1)^2]$ , and  $\gamma_{88} = \partial \bar{\psi}_{cfs}^2 / \partial \bar{I}_{8,fs} \partial \bar{I}_{8,fs} = a_{cfs} \exp[b_{cfs} \bar{I}_{8,fs}^2] (1 + 2b_{cfs} \bar{I}_{8,fs}^2)$ .

### Myocytes

Having defined a one-dimensional constitutive model to characterize the myocytes strain energy function in Eq. (35), the isochoric second Piola-Kirchhoff stress tensor is expressed as follows:

$$\begin{aligned}
\mathbf{S}_{\text{iso, m}} &= 2 \hat{\rho}_m \frac{\partial \bar{\psi}_m(\bar{I}_{4m})}{\partial \mathbf{C}^e} = J^{e-2/3} \text{Dev}(\bar{\mathbf{S}}_m) \\
&= 2 \hat{\rho}_m J^{e-2/3} \text{Dev} \left( \frac{\partial \bar{\psi}_m(\bar{I}_{4m})}{\partial \bar{I}_{4m}} \frac{\partial \bar{I}_{4m}}{\partial \bar{\mathbf{C}}} \right) \\
&= \hat{\rho}_m J^{e-2/3} \gamma_{4m} \text{Dev}(\mathbf{M}_0),
\end{aligned}$$

where  $\gamma_{4m} = \partial \bar{\psi}_m / \partial \bar{I}_{4m} = a_m(\bar{I}_{4m} - 1) \exp[b_m(\bar{I}_{4m} - 1)^2]$ , and we introduce the structural tensor of the myocyte in the undeformed configuration,  $\mathbf{M}_0 = \mathbf{f}_0 \otimes \mathbf{f}_0$ . Note that the latter coincides with the direction of the collagen fiber aligned with the longitudinal axis of the myofiber.

We can finally write the elasticity tensor associated with myocytes:

$$\begin{aligned}
\mathbb{C}_{\text{iso, m}} &= 2 \frac{\partial \mathbf{S}_{\text{iso, m}}}{\partial \mathbf{C}^e} = 4 \hat{\rho}_m \frac{\partial^2 \bar{\psi}_m(\bar{\mathbf{C}})}{\partial \mathbf{C}^e \partial \mathbf{C}^e} \\
&= 4 \hat{\rho}_m \frac{\partial}{\partial \mathbf{C}^e} \left( \gamma_{4m} \frac{\partial \bar{\psi}_m(\bar{I}_{4m})}{\partial \mathbf{C}^e} \right) \\
&= 4 \hat{\rho}_m \left( \gamma_{44,m} \frac{\partial \bar{I}_{4,m}}{\partial \mathbf{C}^e} \otimes \frac{\partial \bar{I}_{4,m}}{\partial \mathbf{C}^e} + \gamma_{4,m} \frac{\partial^2 \bar{I}_{4,m}}{\partial \mathbf{C}^e \partial \mathbf{C}^e} \right) \\
&= 4 \hat{\rho}_m J^{-4/3} \text{Dev} \mathbf{M}_0 \otimes \text{Dev} \mathbf{M}_0 \\
&\quad - 4 \hat{\rho}_m J^{-2/3} \gamma_{4m} \left( \mathbf{C}^{e-1} \otimes \text{Dev} \mathbf{M}_0 + \text{Dev} \mathbf{M}_0 \otimes \mathbf{C}^{e-1} - \bar{I}_{4,m} \tilde{\mathbb{P}} \right),
\end{aligned}$$

where  $\gamma_{44,m} = \partial \bar{\psi}_{c,m}^2 / \partial \bar{I}_{4,m} \partial \bar{I}_{4,m} = a_{c,m} \exp[b_{c,m}(\bar{I}_{4,m} - 1)^2] [1 + 2b_{c,m}(\bar{I}_{4,m} - 1)^2]$ .

## References

- [1] G. Savarese, P. M. Becher, L. H. Lund, P. Seferovic, G. M. Rosano, A. J. Coats, Global burden of heart failure: a comprehensive and updated review of epidemiology (12 2022). doi:10.1093/cvr/cvac013.
- [2] V. Melenovsky, Cardiac adaptation to volume overload (1 2013). doi:10.1007/978-1-4614-5203-4\_9.
- [3] W. Grossman, Cardiac hypertrophy: Useful adaptation or pathologic process? (1980). doi:/10.1016/0002-9343(80)90471-4.
- [4] K. R. Hutchinson, J. A. Stewart, P. A. Lucchesi, Extracellular matrix remodeling during the progression of volume overload-induced heart failure (3 2010). doi:10.1016/j.yjmcc.2009.06.001.
- [5] R. O. Bonow, J. E. Udelson, Left ventricular diastolic dysfunction as a cause of congestive heart failure, pMID: 1503353 (1992). doi:10.7326/0003-4819-117-6-502.
- [6] M. Pathak, S. Sarkar, E. Vellaichamy, S. Sen, Role of myocytes in myocardial collagen production (2001). URL <http://www.hypertensionaha.org>
- [7] J. E. Bishop, G. Lindahl, Regulation of cardiovascular collagen synthesis by mechanical load (1999). URL <https://academic.oup.com/cardiovascres/article/42/1/27/325205>
- [8] K. T. Weber, Cardiac interstitium in health and disease: The fibrillar collagen network (1989). doi:10.1016/0735-1097(89)90360-4.
- [9] M. Nakamura, J. Sadoshima, Mechanisms of physiological and pathological cardiac hypertrophy (7 2018). doi:10.1038/s41569-018-0007-y.
- [10] F. G. Spinale, M. L. Coker, B. R. Bond, J. L. Zellner, Myocardial matrix degradation and metalloproteinase activation in the failing heart: a potential therapeutic target (2000). doi:10.1016/s0008-6363(99)00431-9. URL [www.elsevier.com/locate/cardioreswv.elsevier.nl/locate/cardiores](http://www.elsevier.com/locate/cardioreswv.elsevier.nl/locate/cardiores)
- [11] J. P. M. Cleutjens, Cardiovascular mystery series the role of matrix metalloproteinases in heart disease (1996).
- [12] D. Corporan, D. Onohara, R. Hernandez-Merlo, A. Sielicka, X. M. Padala, Temporal changes in myocardial collagen, matrix metalloproteinases, and their tissue inhibitors in the left ventricular myocardium in experimental chronic mitral regurgitation in rodents (2018). doi:10.1152/ajpheart.00099.2018.-Mitral. URL [www.ajpheart.org](http://www.ajpheart.org)
- [13] T. D. Ryan, E. C. Rothstein, I. Aban, J. A. Tallaj, A. Husain, P. A. Lucchesi, L. J. Dell’Italia, Left ventricular eccentric remodeling and matrix loss are mediated by bradykinin and precede cardiomyocyte elongation in rats with volume overload (2 2007). doi:10.1016/j.jacc.2006.06.083.
- [14] E. C. E. Hajj, M. C. E. Hajj, V. K. Ninh, J. D. Gardner, Inhibitor of lysyl oxidase improves cardiac function and the collagen/mmp profile in response to volume overload (2018). doi:10.1152/ajp. URL [www.ajpheart.org](http://www.ajpheart.org)
- [15] S. Göktepe, S. N. Acharya, J. Wong, E. Kuhl, Computational modeling of passive myocardium (1 2011). doi:10.1002/cnm.1402.
- [16] L. C. Lee, G. S. Kassab, J. M. Guccione, Mathematical modeling of cardiac growth and remodeling (5 2016). doi:10.1002/wsbm.1330.
- [17] W. Kroon, T. Delhaas, T. Arts, P. Bovendeerd, Computational modeling of volumetric soft tissue growth: Application to the cardiac left ventricle (2009). doi:10.1007/s10237-008-0136-z.
- [18] S. Göktepe, O. J. Abilez, E. Kuhl, A generic approach towards finite growth with examples of athlete’s heart, cardiac dilation, and cardiac wall thickening (10 2010). doi:10.1016/j.jmps.2010.07.003.
- [19] M. Genet, L. C. Lee, B. Baillargeon, J. M. Guccione, E. Kuhl, Modeling pathologies of diastolic and systolic heart failure (1 2016). doi:10.1007/s10439-015-1351-2.
- [20] M. Peirlinck, F. Sahli Costabal, K. L. Sack, J. S. Choy, G. S. Kassab, J. M. Guccione, M. De Beule, P. Segers, E. Kuhl, Using machine learning to characterize heart failure across the scales, Biomechanics and Modeling in Mechanobiology 18 (6) (2019) 1987–2001. doi:10.1007/s10237-019-01190-w.
- [21] E. K. Rodriguez, A. Hoger, A. D. Mcculloch, Stress-dependent finite growth in soft elastic tissues (1994).
- [22] J. D. Humphrey, K. R. Rajagopal, A constrained mixture model for growth and remodeling of soft tissues (2002).
- [23] A. M. Gebauer, M. R. Pfäller, J. M. Szafron, W. A. Wall, Adaptive integration of history variables in constrained mixture models for organ-scale growth and remodeling, International Journal for Numerical Methods in Biomedical Engineering 40 (11 2024). doi:10.1002/cnm.3869.
- [24] J. D. Laubrie, S. J. Mousavi, S. Avril, About prestretch in homogenized constrained mixture models simulating growth and remodeling in patient-specific aortic geometries (4 2022). doi:10.1007/s10237-021-01544-3.
- [25] H. Sharifi, C. K. Mann, A. L. Rockward, M. Mehri, J. Mojumder, L.-C. Lee, K. S. Campbell, J. F. Wenk, Multiscale simulations of left ventricular growth and remodeling (2021). doi:10.1007/s12551-021-00826-5/Published. URL <https://doi.org/10.1007/s12551-021-00826-5>
- [26] K. Yoshida, J. W. Holmes, Computational models of cardiac hypertrophy (1 2021). doi:10.1016/j.pbiomolbio.2020.07.001.
- [27] D. Guan, X. Zhuan, X. Luo, H. Gao, An updated lagrangian constrained mixture model of pathological cardiac growth and remodelling (8 2023). doi:10.1016/j.actbio.2023.05.022.
- [28] A. M. Gebauer, M. R. Pfäller, F. A. Braeu, C. J. Cyron, W. A. Wall, A homogenized constrained mixture model of cardiac growth and remodeling: analyzing mechanobiological stability and reversal (12 2023). doi:10.1007/s10237-023-01747-w.
- [29] H. Schmid, L. Pauli, A. Paulus, E. Kuhl, M. Itskov, Consistent formulation of the growth process at the kinematic and constitutive level for soft tissues composed of multiple constituents (5 2012). doi:10.1080/10255842.2010.548325.

[30] A. Goriely, The Mathematics and Mechanics of Biological Growth, Vol. 45, Springer New York, NY, 2017. doi:10.1007/978-0-387-87710-5.

[31] L. C. Lee, J. Sundnes, M. Genet, J. F. Wenk, S. T. Wall, An integrated electromechanical-growth heart model for simulating cardiac therapies, *Biomechanics and Modeling in Mechanobiology* 15 (4) (2016) 791–803. doi:10.1007/s10237-015-0723-8.

[32] P. Sáez, E. Peña, J. M. Tarbell, M. A. Martínez, Computational model of collagen turnover in carotid arteries during hypertension, *International Journal for Numerical Methods in Biomedical Engineering* 31 (2015) 1–20. doi:10.1002/cnm.2705.

[33] F. A. Braeu, S. Avril, M. J. Girard, 3D growth and remodeling theory supports the hypothesis of staphyloma formation from local scleral weakening under normal intraocular pressure, *Biomechanics and Modeling in Mechanobiology* 23 (6) (2024) 2137–2154. doi:10.1007/s10237-024-01885-9.

[34] G. A. Holzapfel, Nonlinear solid mechanics : a continuum approach for engineering, John Wiley & Sons, 2006.

[35] T. S. Eriksson, P. N. Watton, X. Y. Luo, Y. Ventikos, Modelling volumetric growth in a thick walled fibre reinforced artery (12 2014). doi:10.1016/j.jmps.2014.09.003.

[36] A. Grytsan, T. S. Eriksson, P. N. Watton, T. C. Gasser, Growth description for vesselwall adaptation: A thick-walled mixture model of abdominal aortic aneurysm evolution (8 2017). doi:10.3390/ma10090994.

[37] G. A. Holzapfel, R. W. Ogden, Constitutive modelling of passive myocardium: A structurally based framework for material characterization (9 2009). doi:10.1098/rsta.2009.0091.

[38] G. Sommer, A. J. Schriegl, M. Andrä, M. Sacherer, C. Viertler, H. Wolinski, G. A. Holzapfel, Biomechanical properties and microstructure of human ventricular myocardium, *Acta Biomaterialia* 24 (2015) 172–192. doi:10.1016/j.actbio.2015.06.031.

[39] D. Rohmer, A. Sitek, G. T. Gullberg, Reconstruction and Visualization of Fiber and Laminar Structure in the Normal Human Heart from Ex Vivo Diffusion Tensor Magnetic Resonance Imaging (DTMRI) Data, *Investigative Radiology* 42 (11) (2007) 777. doi:10.1097/RLI.0b013e3181238330.

[40] C. Xi, G. S. Kassab, L. C. Lee, Microstructure-based finite element model of left ventricle passive inflation (5 2019). doi:10.1016/j.actbio.2019.04.016.

[41] A. J. Wilson, G. B. Sands, I. J. LeGrice, A. A. Young, D. B. Ennis, Myocardial mesostructure and mesofunction, *American Journal of Physiology - Heart and Circulatory Physiology* 323 (8 2022). doi:10.1152/AJPHEART.00059.2022.

[42] T. Liu, F. Liang, A microstructure-based finite element model of the human left ventricle for simulating the trans-scale myocardial mechanical behaviors (4 2025). doi:10.1016/j.mechmat.2025.105273.

[43] V. Y. Wang, J. A. Niestrawska, A. J. Wilson, G. B. Sands, A. A. Young, I. J. LeGrice, M. P. Nash, Image-driven constitutive modeling of myocardial fibrosis, *International Journal for Computational Methods in Engineering Science and Mechanics* 17 (3) (2016) 211–221. doi:10.1080/15502287.2015.1082675.

[44] E. McEvoy, G. A. Holzapfel, P. McGarry, Compressibility and anisotropy of the ventricular myocardium: Experimental analysis and microstructural modeling (8 2018). doi:10.1115/1.4039947.

[45] D. Guan, F. Ahmad, P. Theobald, S. Soe, X. Luo, H. Gao, On the AIC-based model reduction for the general Holzapfel-Ogden myocardial constitutive law, *Biomechanics and Modeling in Mechanobiology* 18 (4) (2019) 1213–1232. doi:10.1007/s10237-019-01140-6.

[46] P. D. Dale, J. A. Sherratt, P. K. Maini, A mathematical model for collagen fibre formation during foetal and adult dermal wound healing (1996). doi:10.1098/rspb.1996.0098.

[47] Y. F. Jin, H. C. Han, J. Berger, Q. Dai, M. L. Lindsey, Combining experimental and mathematical modeling to reveal mechanisms of macrophage-dependent left ventricular remodeling (5 2011). doi:10.1186/1752-0509-5-60.

[48] M. Sesa, H. Holthusen, C. Böhm, S. Jockenhövel, S. Reese, K. Linka, A comprehensive framework for predictive computational modeling of growth and remodeling in tissue-engineered cardiovascular implants, Arxiv (3 2025). URL <http://arxiv.org/abs/2503.17151>

[49] M. Sesa, H. Holthusen, L. Lamm, C. Böhm, T. Brepols, S. Jockenhövel, S. Reese, Mechanical modeling of the maturation process for tissue-engineered implants: Application to biohybrid heart valves (12 2023). doi:10.1016/j.compbio.2023.107623.

[50] P. Sáez, E. Peña, M. Ángel Martínez, E. Kuhl, Mathematical modeling of collagen turnover in biological tissue (12 2013). doi:10.1007/s00285-012-0613-y.

[51] F. Sahli Costabal, J. S. Choy, K. L. Sack, J. M. Guccione, G. S. Kassab, E. Kuhl, Multiscale characterization of heart failure, *Acta Biomaterialia* 86 (2019) 66–76. doi:10.1016/j.actbio.2018.12.053.

[52] H. Lombaert, J. M. Peyrat, P. Croisille, S. Rapacchi, L. Fanton, F. Cheriet, P. Clarysse, I. Magnin, H. Delingette, N. Ayache, Human atlas of the cardiac fiber architecture: Study on a healthy population, *IEEE Transactions on Medical Imaging* 31 (2012) 1436–1447. doi:10.1109/TMI.2012.2192743.

[53] M. Peirlinck, N. Debusschere, F. Iannaccone, P. D. Siersema, B. Verhegghen, P. Segers, M. De Beule, An in silico biomechanical analysis of the stent–esophagus interaction, *Biomechanics and Modeling in Mechanobiology* 17 (1) (2017) 111–131. doi:10.1007/s10237-017-0948-9.

[54] S. Li, J. Demmel, Superludist: A scalable distributed-memory sparse direct solver for unsymmetric linear systems, *ACM Trans. Math. Softw.* 29 (2003) 110–140. doi:10.1145/779359.779361.

[55] D. Martonová, M. Peirlinck, K. Linka, G. A. Holzapfel, S. Leyendecker, E. Kuhl, Automated model discovery for human cardiac tissue: Discovering the best model and parameters, *Computer Methods in Applied Mechanics and Engineering* 428 (2024) 117078. doi:10.1016/j.cma.2024.117078.

[56] A. P. Voorhees, H. C. Han, Biomechanics of cardiac function, *Comprehensive Physiology* 5 (2015) 1623–1644. doi:10.1002/cphy.c140070.

[57] H. M. Wang, H. Gao, X. Y. Luo, C. Berry, B. E. Griffith, R. W. Ogden, T. J. Wang, Structure-based finite strain modelling of the human left ventricle in diastole, *International Journal for Numerical Methods in Biomedical Engineering* 29 (2013) 83–103. doi:10.1002/cnm.2497.

[58] M. Peirlinck, K. L. Sack, P. De Backer, P. Morais, P. Segers, T. Franz, M. De Beule, Kinematic boundary conditions substantially impact in silico ventricular function, *International Journal for Numerical Methods in Biomedical Engineering* 35 (1) (Oct. 2018). doi:10.1002/cnm.3151.

[59] S. Klotz, I. Hay, M. L. Dickstein, G.-H. Yi, J. Wang, M. S. Maurer, D. A. Kass, D. Burkhoff, Downloaded from journals.physiology.org/journal/ajpheart at TU Delft Lib, *Am J Physiol Heart Circ Physiol* 291 (2006) 403–412. doi:10.1152/ajpheart.01240.2005. –Whereas. URL [www.ajpheart.org](http://www.ajpheart.org)

[60] R. C. Kerckhoffs, J. H. Omens, A. D. McCulloch, A single strain-based growth law predicts concentric and eccentric cardiac growth during pressure and volume overload, *Mechanics Research Communications* 42 (2012) 40–50. doi:10.1016/j.mechrescom.2011.11.004.

[61] D. Zeng, H. Chen, C. L. Jiang, J. Wu, Usefulness of three-dimensional spherical index to assess different types of left ventricular remodeling, *Medicine (United States)* 96 (9 2017). doi:10.1097/MD.0000000000007968.

[62] L. H. Opie, P. J. Commerford, B. J. Gersh, M. A. Pfeffer, Series controversies in cardiology 4 controversies in ventricular remodelling (2006). URL [www.thelancet.com](http://www.thelancet.com)

[63] M. I. Ahmed, E. Andrikopoulou, J. Zheng, E. Ulasova, B. Pat, E. E. Kelley, P. C. Powell, T. S. Denney, C. Lewis, J. E. Davies, V. Darley-Usmar, L. J. Dell’Italia, Interstitial Collagen Loss, Myocardial Remodeling, and Function in Primary Mitral Regurgitation, *JACC: Basic to Translational Science* 7 (10) (2022) 973–981. doi:10.1016/j.jacbs.2022.04.014.

[64] J. L. Emery, J. H. Omens, Mechanical regulation of myocardial growth during volume-overload hypertrophy in the rat (1997).

[65] K. M. Wisdom, S. L. Delp, E. Kuhl, Use it or lose it: multiscale skeletal muscle adaptation to mechanical stimuli (4 2015). doi:10.1007/s10237-014-0607-3.

[66] F. G. Spinale, Myocardial Matrix Remodeling and the Matrix Metalloproteinases: Influence on Cardiac Form and Function, *Physiological reviews* 87 (2007) 1285–1342. doi:10.1152/physrev.00012.2007. URL [www.prv.org](http://www.prv.org)

[67] C. H. Conrad, W. W. Brooks, J. A. Hayes, S. Sen, K. G. Robinson, O. H. L. Bing, Myocardial fibrosis and stiffness with hypertrophy and heart failure in the spontaneously hypertensive rat, *Circulation* 91 (1) (1995) 161–170. doi:10.1161/01.CIR.91.1.161. URL <https://www.ahajournals.org/doi/abs/10.1161/01.CIR.91.1.161>

[68] M. Tanaka, H. Fujiwara, T. Onodera, D.-J. Wu, Y. Hamashima, C. Kawai, Quantitative analysis of myocardial fibrosis in normals, hypertensive hearts, and hypertrophic cardiomyopathy, *British heart journal* 55 (1986) 575–81. doi:10.1136/hrt.55.6.575.

[69] S. Göktepe, O. J. Abilez, E. Kuhl, A generic approach towards finite growth with examples of athlete’s heart, cardiac dilation, and cardiac wall thickening, *Journal of the Mechanics and Physics of Solids* 58 (2010) 1661–1680. doi:10.1016/j.jmps.2010.07.003.

[70] G. J. Perry, C. C. Wei, G. H. Hankes, S. R. Dillon, P. Rynders, R. Mukherjee, F. G. Spinale, L. J. Dell’Italia, Angiotensin II receptor blockade does not improve left ventricular function and remodeling in subacute mitral regurgitation in the dog, *Journal of the American College of Cardiology* 39 (8) (2002) 1374–1379. doi:10.1016/s0735-1097(02)01763-1.

[71] E. Nevo, Y. Lanir, Structural finite deformation model of the left ventricle during diastole and systole, *Journal of Biomechanical Engineering* 111 (4) (1989) 342–349. doi:10.1115/1.3168389. URL <https://doi.org/10.1115/1.3168389>

[72] M. S. Sacks, Incorporation of experimentally-derived fiber orientation into a structural constitutive model for planar collagenous tissues, *Journal of Biomechanical Engineering* 125 (2003) 280–287. doi:10.1115/1.1544508.

[73] V. Y. Wang, P. M. Nielsen, M. P. Nash, Image-based predictive modeling of heart mechanics (12 2015). doi:10.1146/annurev-bioeng-071114-040609.

[74] S. Cardona, M. Peirlinck, B. Fereidoonnehzad, Topogen: topology-driven microstructure generation for in silico modeling of fiber network mechanics (2025). doi:10.48550/ARXIV.2503.19832.

[75] J. M. Guccione, L. K. Waldman, A. D. McCulloch, Mechanics of active contraction in cardiac muscle: Part ii—cylindrical models of the systolic left ventricle, *Journal of Biomechanical Engineering* 115 (1) (1993) 82–90. doi:10.1115/1.2895474. URL <https://doi.org/10.1115/1.2895474>

[76] C. M. Witzenburg, J. W. Holmes, A comparison of phenomenologic growth laws for myocardial hypertrophy, *Journal of Elasticity* 129 (2017) 257–281. doi:10.1007/s10659-017-9631-8.

[77] D. Martonová, M. Peirlinck, K. Linka, G. A. Holzapfel, S. Leyendecker, E. Kuhl, Automated model discovery for human cardiac tissue: Discovering the best model and parameters, *Computer Methods in Applied Mechanics and Engineering* 428 (8 2024). doi:10.1016/j.cma.2024.117078.